Thesis for The Degree of Licentiate of Engineering

Quantification of local lattice distortions in refractory high-entropy alloys by scattering-based techniques

Yao Hu

Department of Physics
Chalmers University of Technology
Gothenburg, Sweden, 2024

Quantification of local lattice distortions in refractory high-entropy alloys by scattering-based techniques

Yao Hu

© Yao Hu, 2024

Department of Physics
Division of Microstructure Physics
Chalmers University of Technology
SE-412 96 Göteborg,
Sweden
Phone: +46 (0)31-772 1000

Cover:
The figure schematically illustrates a synchrotron scattering experiment with a multi-detector setup, examining a powder sample of a high-entropy alloy. The equation at the bottom is the differential scattering cross section.

Printed by Chalmers Digitaltryck,
Gothenburg, Sweden 2024.

Quantification of local lattice distortions in refractory high-entropy alloys by scattering-based techniques

Yao Hu

Department of Physics
Chalmers University of Technology

Abstract

The increasing demand for advanced structural materials for use in extreme conditions, particularly including the aerospace applications, has promoted the development of refractory high-entropy alloys (RHEAs). A deeper understanding of the interaction between microstructure and properties is essential to overcome the scientific challenges associated with these alloys. One notable characteristic of high entropy alloys (HEAs), including RHEAs, is local lattice distortion (LLD) caused by the solid solutioning of multiple principal elements with varying atomic sizes. LLDs generate strain fields that hinder dislocation movement, thus enhancing strength via the solid solution strengthening mechanism.

However, quantifying LLDs in RHEAs poses a challenge due to the subtle nature of these structural changes and a lack of consensus on appropriate methods. The approach of determining average structures of materials through the analysis of X-ray diffraction patterns has been well-recognised. Meanwhile, total scattering technique, along with pair distribution function (PDF), has also shown significant potential in uncovering information at local structure. Both Bragg diffraction and PDF have previously proven effective for the quantitative assessment of LLDs.

In this thesis, it is demonstrated that LLDs in body-centered cubic (BCC) structured RHEAs can be accurately measured through both reciprocal-space Rietveld method and real-space small-box PDF analysis. The obtained LLDs are significantly larger than previously reported values for face-centered cubic (FCC) structured HEAs. Additionally, a comprehensive simulation study explored the effects of chemical segregation, confirming the feasibility of precise LLD determination in RHEAs under specific levels of segregation and LLD. Robust determination of LLDs through small-box PDF analysis is essential for future time-resolved measurements.

Keywords

Refractory high-entropy alloys, local lattice distortion, X-ray diffraction, neutron scattering, total scattering, pair distribution function

List of Publications

Appended papers

This thesis is based on the following papers:

I. **Yao Hu**, Lewis R. Owen, Helen Y. Playford, Aina Edgren, Sheng Guo, Magnus Hörnqvist Colliander, *Quantifying local lattice distortions in refractory high-entropy alloys*,
Submitted to Physical Review Materials

II. **Yao Hu**, Sheng Guo, Magnus Hörnqvist Colliander, *Segregation in refractory high-entropy alloys: Its effect on local lattice distortions derived from pair distribution functions*,
In manuscript

My contributions to the appended papers

I. The neutron and X-ray total scattering experiments were performed by beamline scientists at ISIS (Dr. Helen Playford and Prof. David Keen) and DESY (Dr. Martin Etter and Dr. Henrik S. Jeppesen), as access to facilities were restricted during the COVID pandemic. I performed the high resolution diffraction experiments with assistance from DESY beamline scientists and colleagues. I analysed all scattering and diffraction data, and performed the simulations and fitting of simulated PDFs. Microscopy investigations were performed in collaboration with researchers at Chalmers. As the principal author I wrote the first draft of the manuscript, which was reviewed by Prof. Sheng Guo and Docent Magnus Hörnqvist Colliander with input from co-authors.

II. I did the simulation study with the assistance of Dr. Kristine Bakken and Docent Magnus Hörnqvist Colliander. As the principal author I wrote the first draft of the manuscript, which was reviewed by Prof. Sheng Guo and Docent Magnus Hörnqvist Colliander.

Acknowledgment

Looking back on the past two years since moving to a new country, it has been an amazing journey. I am deeply aware that without the support of many, this experience would not have been possible.

My deepest gratitude goes to my main supervisor, Docent Magnus Hörnqvist Colliander. Thanks for your consistent availability, insightful guidance, and patience in answering my questions. I am especially thankful for your meticulous feedback on my presentations, proposals, manuscripts and this thesis, no matter how late I send them to you. I extend my heartfelt thanks to my co-supervisor, Prof. Sheng Guo, for your thoughtful and flexible supervision. Thank you for your continuous support, guidance, constructive suggestions, and the time you take.

I would like to thank all my colleagues at the Division of Microstructure Physics. Thank you all for creating such a friendly and supportive work environment. It is quite encouraging and I'm sure it will continue with the rest of my PhD. I also want to thank my previous and current office mates, Sezgin and David, for your company during the countless hours spent in the office.

Special thanks to Dr. Michal Strach at CMAL for your assistance with the synchrotron experiment samples, and to Ola Löfgren for your help with IT-related issues. I am particularly grateful to Dr. Lewis Owen for our enlightening discussions and your constructive feedbacks to our paper. Your work has always guided and inspired me. My thanks also to Dr. Helen Playford for conducting the experiments that provided me with quality scattering data at the beginning of this project, and for your support on the data analysis.

I am grateful to be part of the SwedNess graduate school. It gives me the opportunity to participate in courses and training sessions with and learn from enthusiastic PhD peers working with neutrons.

Last but not least, I want to thank my mother and my father for everything they have done for me. All the love and support I received from you has been treasured.

To my dear motherland.

Contents

Chapter 1

Background

1.1 Development of alloys

The development and application of metallic materials have played a critical role throughout the human history (Figure 1.1), and indeed the milestones in the human history are represented by the materials development, such as the Bronze and Iron Ages [1]. Over the past centuries, the invention and utilisation of diverse new metallic materials have substantially driven societal and technological progress. Historically, traditional alloys, which typically consist of one or two primary metallic elements, have been augmented with a minor addition of other metallic or non-metallic elements to achieve desired properties such as high strength, toughness, and anti-radiation characteristics. For instance, steels, often referred to as the "industrial backbone", are fundamentally iron-based, created by incorporating various elements to produce high-strength steels, spring steels, stainless steels, and others, each presenting unique properties within the ferroalloy series. Besides, superalloys, extensively employed in gas turbine engines and beyond, have gone through a continuous development since 1940s because of their unique performance at elevated temperatures [2], [3].

In 2004, a vital breakthrough in the alloy development strategy occurred when Yeh [5] and Cantor [6] reported high entropy alloys (HEAs, or multi-principal element alloys). This innovative class of materials, comprised of five or more elements each present in proportions ranging from 5 % to 35 %, did not form complicated intermetallic compounds but tend to form a single solid solution structure akin to pure metals. This discovery challenged the conventional alloy design concepts, giving rise to a new category of alloys. The unique compositions inherent in HEAs have been demonstrated to possess remarkable mechanical properties (See Figure 1.2), revealing promising applications [7], [8]. Compared to traditional alloys, HEAs with their exceptional compositional and macro-/micro-structural features, make them good candidates in both structural and functional applications.

The innovative approach to alloy design represented by HEAs showcases the ongoing evolution and adaptation within the field of metallurgy. The escalating demands of industrial and daily life applications further emphasize

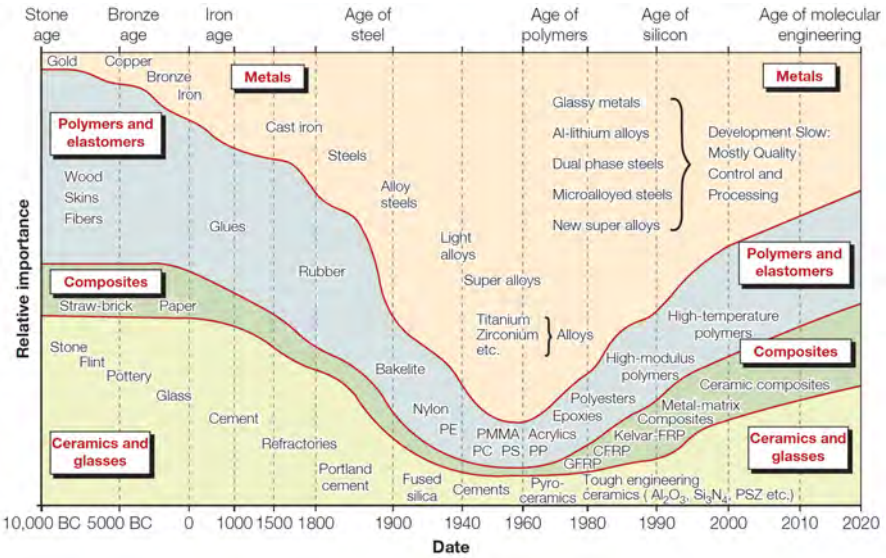

Figure 1.1: The evolution of engineering materials with time [4]. *Reproduced with permission from Royal Society of Chemistry.*

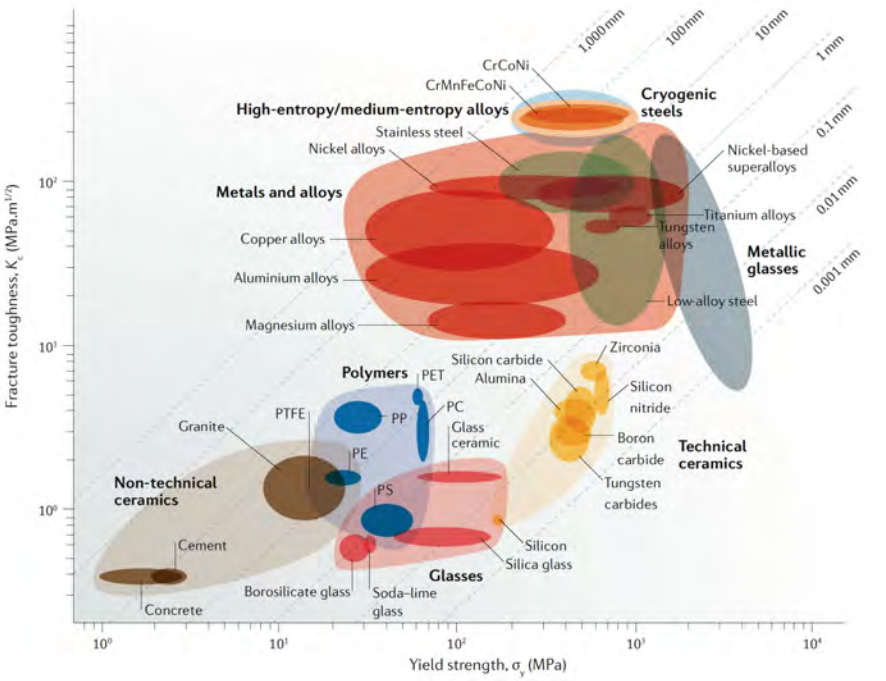

Figure 1.2: Ashby plot of yield strength versus fracture toughness showing the remarkable mechanical properties of representative HEAs among other materials [7]. *Reproduced with permission from Springer Nature.*

the continuous need for optimised metallic materials. With the continuous attention and research from the materials science and condensed matter physics community, the exploration and application of these advanced alloys are bound to push the boundaries of material science, presenting possibilities for future materials and their role in further advancing the human society.

1.2 Gaps and challenges

The pursuit of high-performance structural materials targeting extreme-condition applications, particularly including aerospace, highlights the demand for new high-temperature structural materials with high strength, thermal stability, and oxidation resistance. Despite the superior properties of existing superalloys, their operational temperature is limited, exemplified by Ni-based superalloys, which typically do not exceed 1100°C. Refractory high-entropy alloys (RHEAs) are recently spotlighted as promising candidates for high-temperature applications [9].

One of the primary obstacles in advancing RHEAs is their brittleness at room temperature and limited oxidation resistance at elevated operating temperatures. To address these challenges by developing a novel alloy design strategy for RHEAs, a deeper understanding of the microstructure-properties relationship at the atomic level is required. One frequently referenced mechanism is local lattice distortion (LLD). This phenomenon emerges when the alloying elements, with varying atomic sizes, are introduced into the matrix of the alloy. These elements settle within the crystal structure, creating localized regions with distortion. The resultant strain fields act as barriers, potentially impeding the movement of dislocations. When dislocations find it difficult to move, the material becomes harder and exhibits enhanced mechanical strength. Furthermore, the diverse nature of the elements in RHEAs leads to more pronounced lattice distortions, enhancing the solid solution strengthening effect. Nevertheless, it is noteworthy that similar strengthening effect could also derive from precipitates or other inherent strains within the material. Hence, there is a clear necessity to shed light on this issue.

Beyond that, the challenge of extracting LLDs quantitatively has remained partly due to the difficulty in experimental investigations. Meanwhile, there also remains a debate on the precise definition and metrics for LLDs. Nevertheless, as they are of vital importance for the strengthening and ulteriorly the mechanical properties, it is necessary to dig deeper into this topic.

1.3 Motivation and aim

Despite the significant extent of LLDs within HEAs is expected due to their inherent multi-element nature, it is noteworthy that the enhancement in strength due to LLDs has been observed to be considerably more pronounced in body-centered cubic (BCC) HEAs, including RHEAs [10]–[13]. Thus, controlling LLDs in RHEAs seems to be an effective approach to optimize their mechanical

properties. Yet, a fundamental understanding is lacking, which hinders the strategic design of RHEAs with customised LLDs.

In this thesis the focus will be on the use of scattering techniques for analysis of pair distribution functions (PDFs) obtained from total scattering data. This approach is employed to address key questions about the extent of LLDs in RHEAs and their experimental characterisations:

- How can we accurately quantify LLDs, and are they truly substantial in RHEAs?
- Is total scattering a robust tool for quantifying LLDs?
- How does chemical segregation in dendritic solidification structures impact the accuracy of LLD determination?

The PhD project is a part of the Swedish Graduate School for Neutron Scattering (SwedNess), funded by the Swedish Foundation for Strategic research, which aims at educating the next generation of neutron facility users in order to strengthen the Swedish competence in anticipation of the European Spallation Source (ESS) coming online.

Chapter 2

High-entropy alloys

2.1 Introduction

The term high-entropy alloys (HEAs), usually refers to alloys containing multiple principal elements in equiatomic or near-equiatomic proportions (5 - 35 % as defined in Ref. [5]). While this definition is rooted in the composition of HEAs, it is not restricted to alloys containing five or more elements here since some alloys with only four elements are also sometimes recognized as HEAs in the field.

Another definition is given by the entropy of mixing:

$$\Delta S_{\text{mix}} = -R \sum_{i}^{n} x_i \ln x_i \tag{2.1}$$

where ΔS_{mix} is the entropy of mixing, R the gas constant, x_i the concentration of element i. A general definition considers alloys with $\Delta S_{\text{mix}} \geq 1.5R$ as HEAs. However, this entropy definition can sometimes contradict the composition definition. As a result, these materials are also referred to as multi-principal element alloys (MPEAs) or compositionally complex alloys/complex concentrated alloys (CCAs). Despite these alternative names, "high-entropy alloys" remains the prevalent term. Many researchers believe there is no need to adhere rigidly to the aforementioned definitions for advancing the study of this material.

Over the past twenty years, several characteristics of HEAs have been identified. Among these, the four "core effects" stand out: high entropy, lattice distortion, sluggish diffusion and cocktail effects [14]. These were initially proposed based on early research findings and have since been discussed and evaluated against a more extensive range of published data [8]. In this thesis, the emphasis is placed on the distorted structure.

One of the essential features of HEAs, high entropy, contributes to lower the Gibbs energy and helps to stabilise solid solutions against the formation of intermetallic compounds. Considering the Gibbs free energy of a mixing system:

$$\Delta G_{\text{mix}} = \Delta H_{\text{mix}} - T\Delta S_{\text{mix}} \tag{2.2}$$

Table 2.1: Entropy of equiatomic alloys (ΔS_{mix}) with respect to the type of elements (n). R is the gas constant.

n	1	2	3	4	5
ΔS_{mix}	0	$0.69R$	$1.10R$	$1.39R$	$1.61R$

where ΔG_{mix}, ΔH_{mix} and ΔS_{mix} are the Gibbs free energy, enthalpy and entropy of mixing. For equiatomic alloys (the entropy of the system will be maximised in this case) that contain multiple elements the entropy can be calculated using Equation 2.1, as detailed in Table 2.1. The high mixing entropy typically suggests a reduced probability for ordering and segregation. However, this does not apply to compounds with significantly large (negative) heats of formation, like strong ceramic compounds including oxides, carbides, nitrides, and silicides [5].

Consequently, one can infer that if the magnitude of the entropy could be so pronounced (especially, at high T) that it compensates for the enthalpy of the formation of intermetallic compounds, so that the system tends to form solid solutions to reach the lowest Gibbs energy for stability, as schematically illustrated in Figure 2.1.

2.2 Refractory high-entropy alloys

Single-phase HEAs, exhibiting a range of crystal structures such as FCC (face-centered cubic), BCC (body-centered cubic), and HCP (hexagonal close-packed), have been extensively identified. Among these, one of the first reported

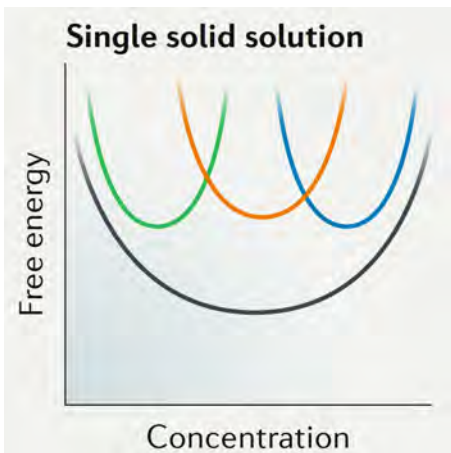

Figure 2.1: Schematic illustrations of the single solid solution feature of HEAs, resulting from the reduction in Gibbs free energy [7]. *Reproduced with permission from Springer Nature.*

Table 2.2: Melting point of some common elements [18] presented in RHEAs.

Element	Ti	Zr	Hf	Nb	Ta	Mo	W
Melting point (K)	1933	2125	2500	2741	3269	2883	3683

HEAs, FCC-structured CrCoFeMnNi (also recognised as the Cantor alloy [6]) along with its derivatives that based on the 3*d*-transition metals (Ti, V, Cr, Mn, Fe, Co, Ni, Cu) have garnered the most attention and research interest. However, the reported HEAs based on transition metals have not shown high-temperature properties or melting points that significantly exceed those of traditional Ni-based superalloys.

This motivates the desire to develop high-temperature alloys inspired by the concept of HEAs. RHEAs were first proposed by Senkov *et al.* in 2010 [17], aiming to develop new high temperature structural materials through the design concept of HEAs. The early RHEAs were typically composed of the refractory elements W, Nb, Mo, Ta, V. As shown in Figure 2.2 (a), with the addition of refractory elements the strength could be improved at high temperatures (over 1000 °C), where the strength of superalloys decreases rapidly.

However, their application is limited due to poor ductility at room temperature, as most BCC (and/or B_2) structured RHEAs show a ductile-to-brittle transition significantly above room temperature [19]. It is reported that adding elements from subgroup IV, such as Hf, Ti, and Zr, typically enhances the ductility of alloys [20], whereas the inclusion of elements such as Cr and Al [21], [22], tends to increase strength at the expense of ductility [23]. Evidence from first principles calculations, as demonstrated by Qi *et al.* [24], suggests that alloying additions can tune the electronic structure of group V and VI metal-

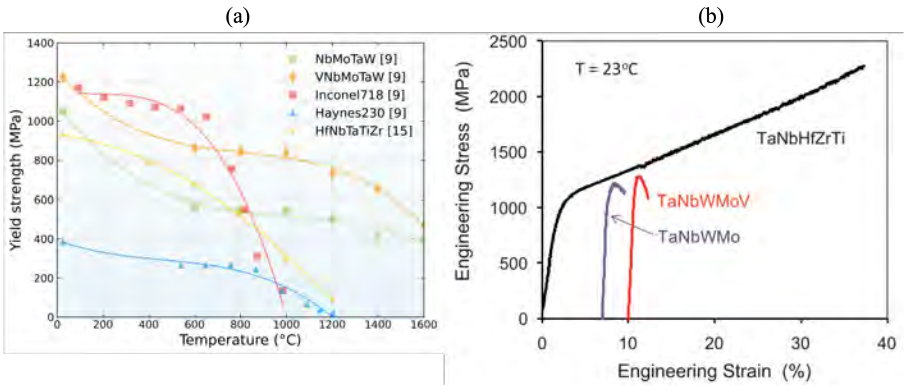

Figure 2.2: Comparative properties of RHEAs: (a) enhanced strength RHEAs in comparison with super alloys at high temperatures [9], [15], and (b) significantly improved ductility of HfNbTaTiZr in comparison with the two initial RHEAs [16]. *Reprinted with permission from Elsevier.*

based RHEAs, and consequently transform their mechanical behaviour from intrinsically brittle to intrinsically ductile. Benefiting from this, HfNbTaTiZr [25], [26] and its derivatives (HfNbTiZr [27], HfTaTiZr [28] etc.) have been some of the most reported RHEAs because of their exceptional balance of strength and ductility, which contributes to its excellent workability, as can be exemplified in Figure 2.2 (b).

Nevertheless, the incorporation of group IV elements introduces additional complexities. Tong *et al.* [29] observed that RHEAs containing Zr and/or Hf elements possess pronounced LLDs, primarily due to the significant size and Fermi level differences between Zr/Hf atoms and other constituent elements through DFT calculations and scattering experiments. Moreover, the melting point difference among the various elements (listed in Table 2.2) often leads to chemical segregation issues. This is evident in the frequently observed dendritic microstructures in as-cast RHEAs [9], [29]–[31], as shown in Fig 2.3.

Therefore, considering the intrinsic LLDs and segregated microstructures in the HfNbTaTiZr RHEA and its derivatives, a thorough investigation is essential. Understanding these features is crucial, not only for enhancing theoretical understanding through advanced analytical techniques, but also for advancing alloy design strategies by tailoring properties aimed at high-performance.

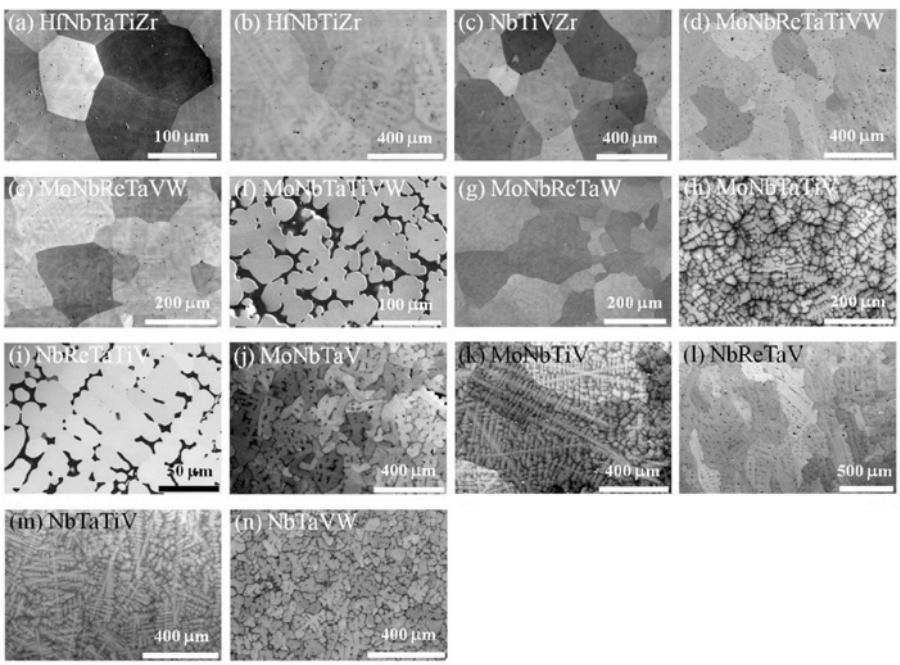

Figure 2.3: Typical dendritic microstructures of some RHEAs in their as-cast state [29]. *Reprinted with permission from Elsevier.*

Chapter 3

Local lattice distortions

3.1 Metrics of LLDs

One significant challenge in the field is the absence of a universally accepted definition for LLDs. One commonly used definition is the atomic size mismatch by considering the deviation of the atomic radii of the individual elements from the mean radius:

$$\delta = \sqrt{\sum_i c_i \left(1 - \frac{r_i}{\bar{r}}\right)^2}, \bar{r} = \sum_i c_i r_i \tag{3.1}$$

Here, c_i and r_i represent the concentration and atomic radius of element i respectively, and $\bar{r}$ stands for the mean atomic radius. It has been suggested from several studies that the LLDs in HEAs with a FCC structure are only slightly greater than in dilute solid solutions [32], [33], while some HEAs with a BCC structure show significantly pronounced LLDs [34]. However, it is noteworthy that for BCC-structured HEAs, LLDs do not consistently align with the value of δ. Even for alloys with comparable δ values, there can be substantial LLD variations [29], [34]. An issue raised here is the lack of consensus on the definition of LLDs (i.e., a suitable metric), and how it should be obtained from the experimental data.

In a recent comprehensive review, Owen and Jones addressed this by proposing terminology and interpretation in this context [35]. Despite the presence of LLDs, the overarching long-range structure of a material remains intact as the average bond length aligns with the lattice parameter, even while individual atoms deviate statically from their ideal lattice sites. Such variations in the local structure are manifested as an expanded range of interatomic distances (bond lengths), a phenomenon observed by *ab initio* studies [34], [36], [37]. Thus, the degree of spread in the interatomic distance distribution, relative to a reference distance, serves as an indicator of local lattice strain. This metric is particularly useful for comparing local structural changes across different materials and correlating findings from various experimental methods.

Though the term "strain" is commonly used in metallurgical contexts, one should clarify that the local lattice strain (or LLD) is distinct from other types

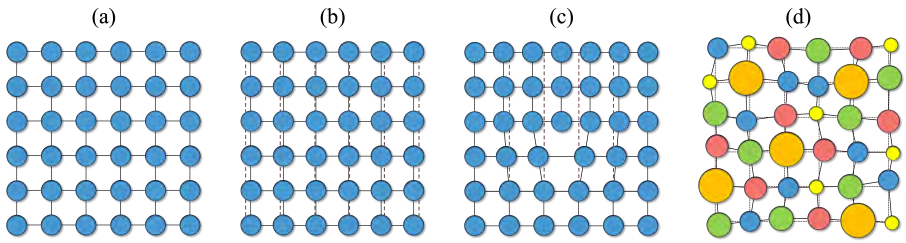

Figure 3.1: Schematic illustrations of different strain types in a 2D lattice, replotted after Owen et al. [38]. The black line represents the actual lattice and the red dashed line denotes the original/perfect lattice, and the blue circles indicate the same atoms. (a) An ideal, strain-free structure. (b) Macrostrain, characterised by an integral change in inter-planar spacing. (c) Microstrain, depicted by shifts in inter-planar spacing near defects. (d) local lattice strains/LLDs, leading to a localised distorted structure while maintaining an average structure, where circles of various colors represent different metallic atoms.

of strains. In line with the classification by Owen [32], the strains therein could be categorised into three types: macrostrain, microstrain and local lattice strain/LLD, each with its unique characteristics and implications in the study of HEAs. To put it simply, a 2D lattice model is used here for illustration. As schematically depicted in Figure 3.1, macrostrain (Figure 3.1 (b)) refers to large-scale or bulk deformations across the entire structure, typically resulting in global changes in the alloy's shape or volume, such as stretching, compression, or bending, and leads to variations in inter-planar spacing overall. In contrast, microstrain (Figure 3.1 (c)) refers to small-scale deformation around specific areas like defects, dislocations, or grain boundaries, causing slight variations in the inter-planar spacing within the crystal structure. The LLDs (Figure 3.1 (d)) are the static displacements of atoms from their ideal lattice sites (See 3.2), in order to accommodate the size differences among atoms. It should be noted that despite the presence of LLDs, the overall crystal structure of the HEAs remain intact, as evidenced by the Bragg peaks observed in its diffraction pattern. These distortions are not significant enough to transform the crystalline structure into an amorphous form, thus preserving the HEA's crystallinity [38].

3.2 Effects of LLDs on properties and structures of HEAs

The impact of LLDs on RHEAs, primarily manifested as enhanced solid solution strengthening, has been extensively documented in numerous studies. Wang et al. [10] linked the notable strengthening in $TiNbTaZrHf_{0.122}$ to lattice distortions that markedly impede the dislocation movement. Similarly, Lee et al. [39] observed that homogenizing NbTaTiV RHEA induces LLDs, resulting in

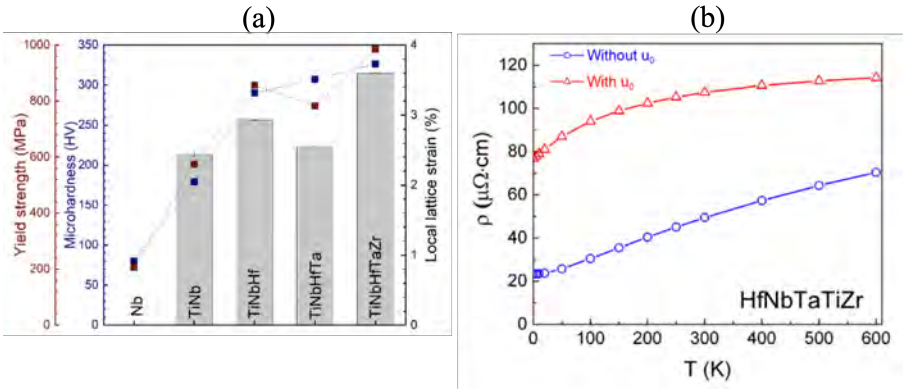

Figure 3.2: The effects of LLDs on (a) enhancing solid solution strengthening [11] (*Reprinted with permission from Elsevier*), and (b) increasing electrical resistivity [40] (u_0 denotes static displacements in this plot) (*Reprinted with permission from Elsevier*).

solid-solution hardening as the main strengthening mechanism, primarily due to the lattice distortion during deformation. Also, Lee et al. [13] identified lattice distortion as a key driver of solid solution strengthening in both NbTaTiV and NbTaTiVZr. In the TiNbHfTaZr HEA system, Thirathipviwat et al. [11] reported a correlation between pronounced lattice distortion and increased solid solution strengthening, as illustrated in Figure 3.2 (a).

Furthermore, in contrast to conventional BCC metals, some studies suggest that LLDs may play a role in controlling the edge dislocations and consequently increasing strain hardening of BCC-structured RHEAs [41]–[43]. Rao et al. [44] explored dislocation behavior in a BCC $Co_{16.67}Fe_{36.67}Ni_{16.67}Ti_{30}$ alloy, noting that the presence of Ti as a significant misfit strain center contributes to the variability in core structures along dislocation lines for both screw and edge dislocations. Similarly, there is emerging evidence that LLDs might impact the relative velocity of edge and screw dislocations [45]. In addition, *ab initio* calculations have also shown that LLDs play a fundamental role in the stability of the BCC phase, as the effect of the static displacement mimics dynamic thermal vibrations and thus effectively stabilizes the high-temperature stable BCC phase over the low-temperature stable HCP structure [46].

Beyond this, other physical properties such as electrical transport can be affected by LLDs. Mu et al. [40] showed that the electronic density of states in several BCC-structured RHEAs (HfNbTiZr, VCrZrNb, HfNbTaTiZr, and CrNbTiVZr) can be modified substantially by LLDs and the corresponding resistivity is raised (as shown in Figure 3.2 (b)). Furthermore, a recent theoretical study by Jasiewicz et al. [47] theoretically revealed that the superconducting critical temperature in $(TaNb)_{0.67}(HfZrTi)_{0.33}$ is halved, highlighting the influence of structural disorder on superconductivity. The superconducting property was already reported experimentally on a derivative of this RHEA $Ta_{34}Nb_{33}Hf_8Zr_{14}Ti_{11}$ [48].

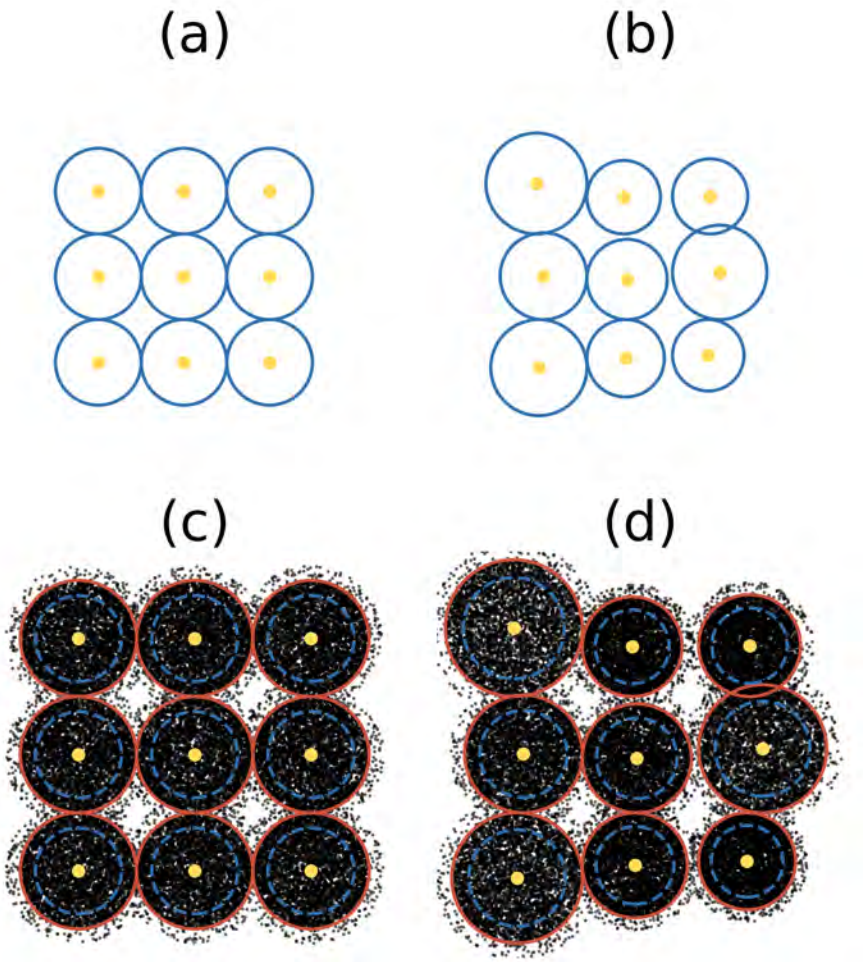

Figure 3.3: Schematic illustration of atomic displacements in materials, replotted after Owen et al. [35]. yellow points: the average positions of atomic centers, blue circles: hard sphere atoms in the absence of thermal vibrations, red circles: hard sphere atoms experiencing thermal vibrations, black dots: the positions of atomic centres over time. The four subplots describe the behaviour of atoms under various conditions: (a) without static and thermal displacements, (b) with static displacements only, (c) with thermal displacements only, (d) with both static and thermal displacements.

To elucidate the impact of LLDs on material properties, it is necessary to examine the structural variations they induce [35]. Figure 3.3 provides a schematic representation of atomic displacements, encompassing both thermal and static components. Imagine a perfect 2D structure at 0 K (no energy presented), where all atoms (yellow points) occupy their precise lattice sites, exhibiting no displacement, as clearly illustrated in the corresponding hard-sphere model (blue circles) shown in Figure 3.3 (a). Upon the introduction of static displacements, the lattice experiences slight distortion, with atoms deviating from their ideal positions, as shown in Figure 3.3 (b). Again, in this state, the atoms remain stationary due to the absence of energy. However, with an increase in temperature, the atoms begin to exhibit vibrational motion (black dots) and occupy a larger volume (red circles). This thermal motion leads to thermal displacements, causing the average atomic distribution (yellow points) to spread further apart, as shown in Figure 3.3 (c). In scenarios where both thermal and static displacements coexist (Figure 3.3 (d)), the lattice not only becomes distorted but also experiences an increased separation between the atoms.

3.3 Determination of LLDs

As discussed in Section 3.2, the static displacements (LLDs) could be described as the variation in the distribution of interatomic distances (i.e., atomic offsite displacements). A method of determining LLDs is discussed in this section. In addition, considering that static displacements are typically convoluted with thermal displacements under normal conditions (at temperatures $T > 0$ K), methodologies on how to separate these two types of displacements are also discussed.

3.3.1 Definition of local lattice strain

This section briefly recapitulates the methodology and terminology proposed by Owen and Jones [35], [38]. As shown in Figure 3.3 (b), the LLDs, depicted as static displacements, could be described as the statistical distribution of the atomic radius by its change in standard deviation $\sigma_{\mathrm{s,u}}$ (here the subscript s indicates that it is the distribution of static displacements, and u indicates that it is the distribution of offsite displacements that is considered) compared to the average atomic radius $\bar{r}$:

$$\varepsilon_{\mathrm{s,u}} = \frac{\sigma_{\mathrm{s,u}}}{\bar{r}}. \tag{3.2}$$

Note that this definition is actually consistent with the one used for atomic size mismatch δ in Eq. 3.1 (however, it is a somewhat rough calculation as other effects e.g., charge transfer effects would not be included) as:

$$\delta = \sqrt{\sum_i c_i \left(1 - \frac{r_i}{\bar{r}}\right)^2} = \frac{1}{\bar{r}} \sqrt{\sum_i c_i \left(\bar{r} - r_i\right)^2} = \frac{\sigma_r}{\bar{r}}. \tag{3.3}$$

Assuming a hard-sphere model for BCC-structured RHEAs, the average atomic radius $\bar{r}$, could be calculated from the lattice parameter a:

$$\bar{r} = \frac{\sqrt{3}}{4}a. \tag{3.4}$$

For the majority of metals, where the strain field tends to be isotropic, the offsite displacement could be effectively represented using a Gaussian distribution as:

$$f(u_s) = \frac{1}{\sigma_{\mathrm{s,u}}\sqrt{2\pi}} \exp\left\{-\frac{1}{2}\left(\frac{u_s - \mu_{\mathrm{s,u}}}{\sigma_{\mathrm{s,u}}}\right)^2\right\} \tag{3.5}$$

where u_s is the static displacement and $\mu_{\mathrm{s,u}} = 0$ as the mean. For a Gaussian distribution we also have $\sigma^2_{\mathrm{s,u}} = u_s^2 = U_s$, where U_s is the isotropic atomic static displacement parameter.

Alternatively, one can consider the statistical distribution of interatomic distances by its change in standard deviation $\sigma_{\mathrm{s,l}}$ (here l refers to the interatomic distances), relative to the average bond length (μ_l), according to

$$\varepsilon_{\mathrm{s,l}} = \frac{\sigma_{\mathrm{s,l}}}{\mu_l}. \tag{3.6}$$

Similarly the distribution of interatomic distances is given as:

$$f(l) = \frac{1}{\sigma_{\mathrm{s,l}}\sqrt{2\pi}} \exp\left\{-\frac{1}{2}\left(\frac{l - \mu_l}{\sigma_{\mathrm{s,l}}}\right)^2\right\} \tag{3.7}$$

The two are directly related as $\mu_l = 2\bar{r}$ in the hard-sphere approximation. Additionally, since the two atoms involved in the bond length measurement each have offsite displacements, so we have $\sigma^2_{\mathrm{s,l}} = \sigma^2_{\mathrm{s,u}} + \sigma^2_{\mathrm{s,u}}$, hence $\sigma_{\mathrm{s,l}} = \sqrt{2}\sigma_{\mathrm{s,u}}$. In the following we have used $\varepsilon_{\mathrm{s,u}}$ to represent the LLDs. Thus, σ_s and ε_s hereafter refer to $\sigma_{\mathrm{s,u}}$ and $\varepsilon_{\mathrm{s,u}}$, respectively.

3.3.2 Separating thermal displacements

This section briefly recapitulates the methodology and terminology proposed by Owen et al. [33]. As we discussed earlier, the static displacements are convoluted with thermal displacements, so any experimental measurements could lead to composite results of both components. To distinguish between these two contributions, separation is essential. The most precise method for this involves conducting variable-temperature measurements at cryogenic conditions. However, this approach may not always be practical in various scenarios, and the time-intensive nature of these measurements could be another challenge. Consequently, in such situations, it becomes necessary to resort to approximate methods for estimating the thermal component.

Similar to Eq. 3.5, thermal displacements could be described in the form of Gaussian distribution as:

$$f(u_t) = \frac{1}{\sigma_t\sqrt{2\pi}} \exp\left\{-\frac{1}{2}\left(\frac{u_t - \mu_t}{\sigma_t}\right)^2\right\} \tag{3.8}$$

the total displacement is then:

$$f(u) = \frac{1}{\sigma_u\sqrt{2\pi}} \exp\left\{-\frac{1}{2}\left(\frac{u-\mu}{\sigma_u}\right)^2\right\} \tag{3.9}$$

where $\sigma_u^2 = \sigma_s^2 + \sigma_t^2$. For metallic alloys, displacements are isotropically distributed, thus,

$$U = U_s + U_t \tag{3.10}$$

where $U_s = \sigma_s^2$ and $U_t = \sigma_t^2$. Subsequently, we have

$$\sigma_s = \sqrt{U - U_t} \tag{3.11}$$

The question is now how to determine U and U_t. In diffraction techniques, the displacement parameters (usually shown as U_{iso} in the scattering community) could be extracted by refining the experimental diffraction pattern (more details in Chapter 4). But again, these techniques measure the combined effect of thermal vibrations and LLDs (i.e., U in Eq. 3.10), so it is important to subtract U_t. An intuitive way to estimate thermal components without measurements is discussed in Section 6.1.

Chapter 4

Measuring LLDs

4.1 Common techniques

4.1.1 TEM

Transmission Electron Microscopy (TEM) is a sophisticated tool for investigating the microstructure of materials at a refined scale, offering good spatial resolution that enables the observation of localised strains at atomic length scales. Among the TEM-based methodologies for strain measurement, dark field electron holography (DFEH) is noted for its precision [49], although its functionality is markedly affected by sample thickness and the necessity for a strain-free reference area, makes it less suitable for studying LLDs in HEAs. High-resolution transmission electron microscopy (HRTEM) is recognised as its exceptional spatial resolution ($\sim$ 0.03 Å) [50], yet it is likewise sensitive to sample thickness, potentially leading to artefacts. Nanobeam electron diffraction (NBED) offers an advantage of measuring without a reference area [51], while challenges of this method include its potential inaccuracies as the diffraction spots are collected pointwise, as well as compromising spatial resolution ($\sim$ 1 nm). A significant concern for these TEM methods is the necessity for sample thinning, which may induce relaxation of the material, thereby reducing the original level of strains. Consequently, accurately quantifying LLDs from a thinned sample becomes challenging due to the need to account for the thin-film effect. Hÿtch et al. [52] proposed that the thinning process introduces two free surfaces absent in the bulk sample, which can relax some of the stresses and strains, typically by about 10 %. Hence, these methods might not be ideal for HEAs, where accurate analysis depends critically on measurements from bulk materials.

4.1.2 EXAFS

Another notable tool for probing local structure is Extended X-ray Absorption Fine Structure (EXAFS). A key advantage of EXAFS lies in its provision of direct access to real space which provides element-specific information [53]–[55]

of the local coordination environment e.g., coordination atom, coordination number and interatomic distance (which makes it possible to measure μ_l in Eq. 3.6) etc. However, this specificity can also introduce challenges, especially in the context of HEAs where multiple elements are involved. Each atom type requires separate measurements, potentially complicating the experiments. Additionally, only up to the first two coordination shells are generally considered effective. Another concern is that in materials like HEAs, the element-unique absorption edges of the atoms might be closely spaced in energy if their electronic structures are similar, which could then affect the effectiveness of this technique. Nevertheless, when these challenges are manageable, it should be possible to assess the distribution of bond lengths around atoms of different types and so can extract $\varepsilon_{s,l}$ in Eq. 3.6 [35].

4.2 Scattering approaches

In the century following the groundbreaking discovery that crystals can diffract X-rays, the practice of determining structures through the analysis of scattering patterns has evolved into a broadly used and definitive technique. Through the analysis of diffraction patterns, the average structure of a material can be determined.

Consider a beam is incident on and subsequently scattered by an object, as shown in Figure 4.1, the incident and scattered beams can be represented by vectors $\mathbf{k}_i$ and $\mathbf{k}_j$. The scattering vector $\mathbf{Q}$ is defined as the difference between these two vectors,

$$\mathbf{Q} = \mathbf{k}_i - \mathbf{k}_j \tag{4.1}$$

From $\mathbf{Q}$ the scattering amplitude $\Psi(\mathbf{Q})$ is defined as:

$$\Psi(\mathbf{Q}) = \frac{1}{\langle b \rangle} \sum b e^{i\mathbf{Q}\cdot\mathbf{R}}, \tag{4.2}$$

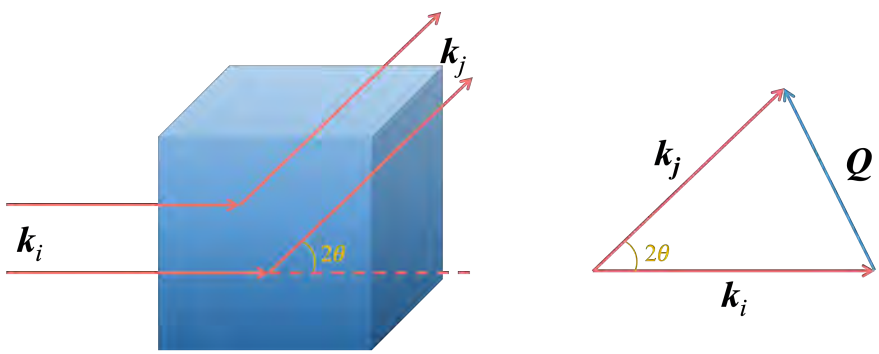

Figure 4.1: Schematic illustration of scattering from an object and the relationship between the incident vector $\mathbf{k}_i$, scattered vector $\mathbf{k}_j$ and scattering vector $\mathbf{Q}$.

where b is the scattering length. For X-rays, b depends on Q, but for neutrons b is independent of Q. The angle brackets denote the average value. $\mathbf{R}$ is the atomic position. However, scattering amplitude is not measurable in practice. Alternatively we measure the scattering intensity, which is related to the differential scattering cross section from the square of the magnitude of $\Psi(\mathbf{Q})$:

$$\frac{\mathrm{d}\sigma(\mathbf{Q})}{\mathrm{d}\mathbf{\Omega}} = \frac{\langle b\rangle^2}{N}|\Psi(\mathbf{Q})|^2 = \frac{1}{N}\sum_{i,j} b_i b_j \mathrm{e}^{\mathrm{i}\mathbf{Q}\cdot(\mathbf{R}_i-\mathbf{R}_j)} \tag{4.3}$$

where σ is the total number of scattered particles (neutrons or photons in X-rays), $\mathbf{\Omega}$ the solid angle, $\frac{\mathrm{d}\sigma(\mathbf{Q})}{\mathrm{d}\mathbf{\Omega}}$ denotes the number of particles scattered into solid angle per second from all incident particles, N the number of atoms scattered the beam in the object, i and j refer to different atoms. The scattering intensity ($I(\mathbf{Q})$) is a normalised form of the differential cross section:

$$I(\mathbf{Q}) = \frac{\mathrm{d}\sigma}{\mathrm{d}\mathbf{\Omega}} + \langle b\rangle^2 - \left\langle b^2\right\rangle = \langle b\rangle^2 S(\mathbf{Q}) \tag{4.4}$$

where $S(\mathbf{Q})$ is the scattering structure function,

$$S(\mathbf{Q}) = \frac{1}{\langle b\rangle^2}\frac{\mathrm{d}\sigma}{\mathrm{d}\Omega} - \frac{\left\langle b^2\right\rangle - \langle b\rangle^2}{\langle b\rangle^2} \tag{4.5}$$

4.2.1 Bragg diffraction

If the object is crystalline, constructive interference occurs when Laue condition is fulfilled, which results in strong interference maxima at specific $\mathbf{Q}$, denoted as

$$\mathbf{Q} = \mathbf{G} \tag{4.6}$$

where $\mathbf{G}$ is a reciprocal lattice vector. This type of scattering was noted by Bragg that the amplifying scattering in 1D diffraction patterns happens at scattering angle θ satisfying the condition:

$$n\lambda = 2d\sin\theta \tag{4.7}$$

where λ is the wavelength of the incident wave, d the interplanar spacing. This is commonly known as "Bragg's Law".

Note that the intensity of Bragg diffraction is composed of two main components: intensity from sample and background intensity, simply denoted as:

$$I = I_{\text{sample}} + I_{\text{background}} \tag{4.8}$$

where the background intensity includes various components, e.g., instrumental contributions, fluorescence, multiple scattering and diffuse scattering etc. In practice, background intensity can complicate the interpretation of diffraction patterns and needed to be subtracted. This is usually done using a polynomial function to remove the signal underneath the Bragg peaks.

4.2.2 Diffuse scattering

Traditional crystallography operates under the premise that crystals are composed of a three-dimensional repetitive lattice of identical units. However, real-world materials often diverge from this idealised model, and their diffraction patterns usually exhibit not only sharp Bragg peaks. As has already been discussed in Section 4.2.1, the Bragg diffraction only includes a specific part of the scattering where constructive interference happens. However, those waves also scattered but not in phase due to the imperfect structure of the material will also yield scattering intensity, which is denoted as diffuse scattering (I_{diffuse}) derived from the sample:

$$I = I_{\text{Bragg}} + I_{\text{diffuse}} + I_{\text{background}} \tag{4.9}$$

It should be noted here the background intensity here differs from that in Eq. 4.8, in which the diffuse scattering is considered as part of the background.

Diffuse scattering spans the entire scattering range Q and usually exhibits as a weak, continuous background, in contrast to Bragg diffraction which occurs exclusively at specific points where the Bragg condition is met (Eq. (4.7)). This phenomenon is indicative of any deviations from the perfect crystal structure. The characteristics of many materials depend not merely on the average crystal structure inferred from Bragg diffraction analysis but are critically influenced by the imperfections or disorder revealed through diffuse scattering analysis. Although diffuse scattering has been a subject of study since the inception of crystallography, it has mostly been explored by a limited number of specialized research teams due to the generally low signal intensity. Nevertheless, the recent emergence of synchrotron radiation sources, advanced high-resolution and high-covered-range X-ray detectors, along with powerful computational tools for analysis and modeling, have significantly mitigated the challenges that once hindered the progress in diffuse scattering techniques.

4.2.3 Total scattering

Total scattering includes the information of both long-range order from Bragg peaks (average structure) and short-range order from diffuse scattering. The analysis of total scattering pattern has recently been applied in studying disordered crystalline and nano-crystalline materials. The total scattering and PDF nomenclatures used in this thesis are mainly from Egami and Billinge [56]. As defined by the scattering structure function in Eq. 4.5, the reduced structure function $F(Q)$ can be easily expressed as:

$$F(Q) = Q[S(Q) - 1] \tag{4.10}$$

By applying a sine transform to $F(Q)$, the reduced pair distribution function can be derived from reciprocal-space data, transforming the information from reciprocal-space into real-space:

$$G(r) = \left(\frac{2}{\pi}\right) \int_0^\infty F(Q) \sin(Qr) \mathrm{d}Q. \tag{4.11}$$

However, reaching zero or infinity in Q is not feasible in practical experiments. So the equation is modified to account for the limited range of Q:

$$G(r) = \left(\frac{2}{\pi}\right) \int_{Q_{\min}}^{Q_{\max}} F(Q) \sin(Qr) \mathrm{d}Q, \tag{4.12}$$

The reduced pair distribution function $G(r)$ can also be defined in terms of the density function:

$$G(r) = 4\pi r \left[\rho(r) - \rho_0\right] = 4\pi r \rho_0 [g(r) - 1], \tag{4.13}$$

where $\rho(r)$ is the atom-pair density function, $g(r)$ the pair distribution function derived from the Fourier transform of the structure function $S(Q)$, and ρ_0 the atomic number density of N atoms in the volume V ($\rho_0 = N/V$).

In multicomponent systems, which comprise more than one type of atom and represent the majority of practical cases, the calculation of the reduced pair distribution function $G(r)$ requires a modification:

$$G_{\alpha\beta}(r) = \sum_{\alpha} \sum_{\beta} W_{\alpha\beta} G_{\alpha\beta}(r) = 4\pi r \rho_0 \sum_{\alpha} \sum_{\beta} [g_{\alpha\beta}(r) - 1], \tag{4.14}$$

where $G_{\alpha\beta}(r)$ is the partial reduced pair distribution function, and

$$W_{\alpha\beta} = c_\alpha c_\beta \frac{b_\alpha b_\beta}{\langle b \rangle^2}, \tag{4.15}$$

is the weighting, and the measured PDF is the weighted sum of the different partial PDFs.

It is worth noting that $G(r)$ is often normalized further to remove the scaling arising from the atomic concentrations and scattering lengths. Moreover, different formalisms have been used in different software. To avoid confusion, alternative normalizations and formalisms can be found in Ref. [57].

4.2.4 PDF

The pair distribution function (PDF) is a histogram of the distribution of interatomic distances, weighted by scattering length, as schematically illustrated in Figure 4.2. Peaks in the PDF, corresponding to various distances, represent different atomic shells (marked in different colours in Figure 4.2) surrounding an atom. The position of these peaks (r) is indicative of bond lengths, while their intensity is related to the coordination number, i.e., the number of neighbouring atoms at a specific distance. Additionally, the peak width reveals the variation of bond lengths, from which the off-site displacements of atoms could be extracted.

Historically, PDF analysis was primarily used for characterizing the structure of disordered materials, with limited application in the study of crystalline materials. However, the advent of synchrotron X-ray radiation and spallation neutron sources has markedly improved the quality of data available across a broad Q range. This enhancement has made PDF analysis a powerful tool for

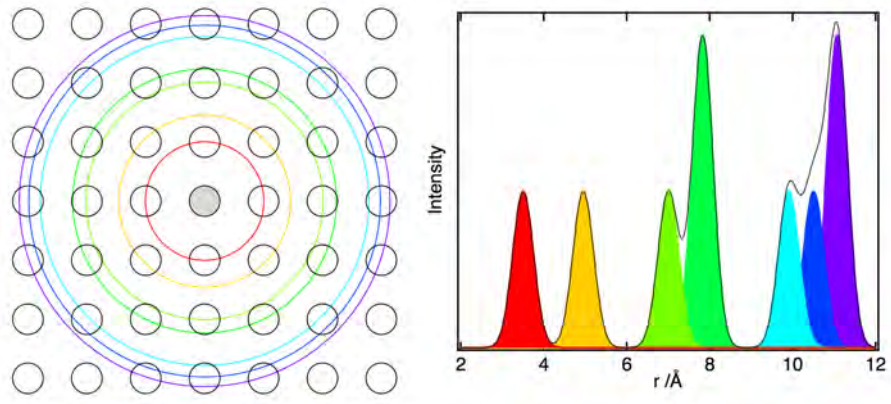

Figure 4.2: Schematic illustration of a PDF calculated from a 2-D lattice [38]. *Reproduced with permission from SNCSC.*

probing atomic-scale structures. Unlike EXAFS, which offers more localised information, total scattering and PDF analysis are bulk techniques that yield information on local structures over larger distances. This capability facilitates more accurate data fitting and provides a comprehensive view of a material's microstructure.

4.2.5 The effect of LLDs on scattering

Since the scattering technique is the primary tool used in this thesis, it is both pertinent and interesting to explore the effects that LLDs may apply on Bragg diffraction and on PDF.

4.2.5.1 From Bragg diffraction

The LLDs could be considered as a deviation ($\mathbf{u}$) of the atomic position from the average position $\bar{\mathbf{R}}$, $\mathbf{R} = \bar{\mathbf{R}} + \mathbf{u}$. Eq. 4.3 will now be:

$$S(\mathbf{Q}) = \frac{1}{N}\sum_{i,j} b_i b_j e^{i\mathbf{Q}[(\bar{\mathbf{R}}_i+\mathbf{u})-(\bar{\mathbf{R}}_j+\mathbf{u})]} \tag{4.16}$$

For simplicity, deriving only the exponential part, the above Eq. reduced to

$$e^{i\mathbf{Q}\bar{\mathbf{R}}_i[1+i\mathbf{Q}\mathbf{u}-\frac{1}{2}(\mathbf{Q}\mathbf{u})^2+\ldots]-i\mathbf{Q}\bar{\mathbf{R}}_j[1+i\mathbf{Q}\mathbf{u}-\frac{1}{2}(\mathbf{Q}\mathbf{u})^2+\ldots]} \approx e^{i\mathbf{Q}(\mathbf{R}_i-\mathbf{R}_j)} \cdot e^{-\mathbf{Q}^2\mathbf{u}^2} \tag{4.17}$$

where $e^{-\mathbf{Q}^2\mathbf{u}^2} = e^{-2W}$, e^{-W} is usually called the Debye-Waller factor, a common way to write this is:

$$e^{-\mathbf{Q}^2\mathbf{u}^2} = e^{-2B(\frac{\sin\theta}{\lambda})^2}, B = 8\pi^2 u^2 \tag{4.18}$$

where B is the B-factor. In diffraction, the effect of atomic displacements is to reduce the intensity of the Bragg peak as illustrated in Figure 4.3 (a).

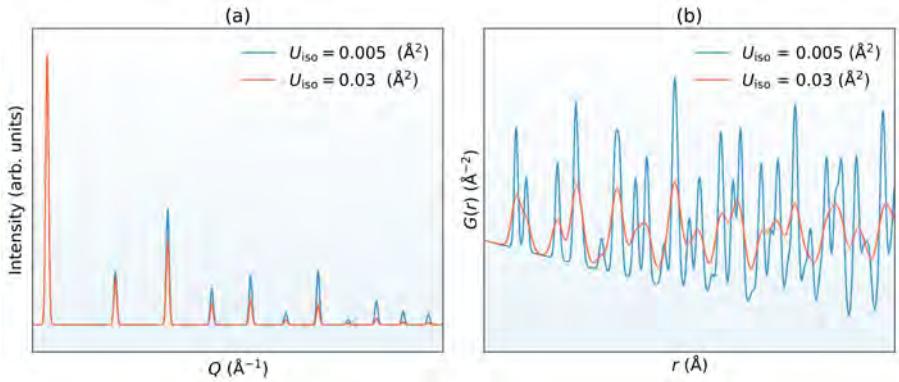

Figure 4.3: (a) Scattering angle-dependent decay of the diffraction peak intensity due to displacements. (b) Broadening PDF peaks with larger U_{iso} values.

4.2.5.2 From PDF

As is well-known that atoms within materials will vibrate from their ideal locations at temperatures above 0 K. These thermal vibrations cause displacements convoluted with static displacements (LLDs), and could be described as a statistical distribution. This distribution reflects the level of deviation of atoms displaced from their idealised positions, where the variance of static and thermal displacements are denoted by σ_{s}^2 and σ_{t}^2 respectively, with σ_{s} and σ_{t} being the standard deviations of static and thermal displacements.

In scattering experiments, the combined effect of these displacements is captured by the derived isotropic displacement parameter U_{iso}, including both static (U_{s}) and thermal (U_{t}) components:

$$U_{\text{iso}} = U_{\text{s}} + U_{\text{t}} = \sigma_{\text{s}}^2 + \sigma_{\text{t}}^2 \tag{4.19}$$

Specifically, in real-space PDFs, increase in U_{iso} due to the presence of off-site displacements leads to an increase in the peak width $\sigma(r)$, as shown in Figure 4.3 (b). This phenomenon is mathematically modelled as [58], [59]:

$$\sigma(r) = \sqrt{U_{\text{iso}} \left(1 - \frac{\delta_1}{r} - \frac{\delta_2}{r^2} + Q_{\text{broad}}^2 r^2\right)} \tag{4.20}$$

where δ_1 and δ_2 are correction factors for peak narrowing at small r values, addressing the effects of correlated motion. The term Q_{broad} accounts for the broadening of PDF peaks due to the instrumental resolution.

Chapter 5

Experimental and data processing

5.1 Materials and microstructure

HfNbTaTiZr was obtained in the form of gas atomized powders. Ingots of the initial HfNbTaTiZr alloy were prepared by arc-melting of blends of pure metals with $>$ 99.9 wt.% purity placed in a water-cooled copper crucible, under protective Helium atmosphere. To mix the elements in the melt pool properly and to homogenize the produced material, the ingot was flipped and repeatedly remelted (eight times). The ingots were subsequently gas atomized into powder by electrode induction-melting gas atomization in a crucible-free process under protective Ar atmosphere to suppress undesirable oxidation of the material. The particle size distribution of the powder is 17–277 μm (Dv10-Dv90). Every powder particle contains numerous equiaxed grains, and the average diameter of these grains is 9.5 $\pm$ 2.9 μm [30]. The microstructure of the powder was characterised using energy-dispersive X-ray spectroscopy (EDS) in a scanning electron microscope (FEI Quanta 200 FEG ESEM operated at 10 kV). Back-scatter electron (BSE) imaging was performed at 10 kV to obtain

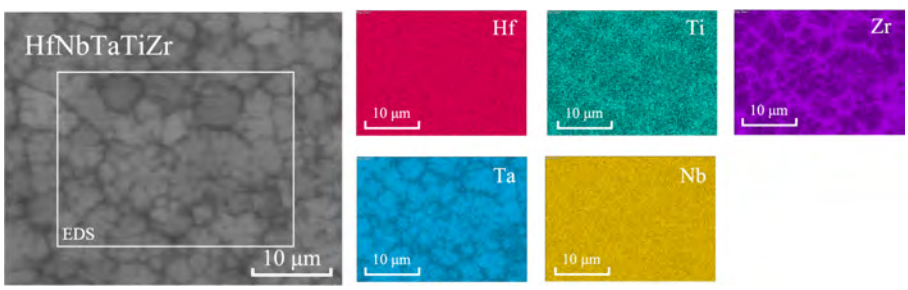

Figure 5.1: Dendritic microstructure of a HfNbTaTiZr powder sample showed by SEM and EDS.

Table 5.1: Chemical composition in atomic percent (at.%) of HfNbTaTiZr from EDS.

Element	**Hf**	**Nb**	**Ta**	**Ti**	**Zr**
Bulk	20.49(6)	19.0(2)	20.3(5)	22.3(2)	17.9(5)
Dendrite	19.0(3)	21.6(4)	27.9(6)	18.8(5)	12.7(4)
Inter-dendrite	21.0(4)	15.1(6)	11(1)	27.4(8)	25(1)

high resolution chemical contrast. A BSE image of the microstructure and the corresponding EDS maps are shown in Figure 5.1. A dendritic microstructure can be clearly observed, indicating the presence of chemical segregation within the material. This is similar to the as-cast material as shown in Figure 2.3. The chemical composition was determined by EDS analysis and listed in Table 5.1. The bulk values were derived from averaging two map scans, while the dendrite and inter-dendrite values were obtained from point scans, averaging 10 and 9 points respectively. Significant variations in elemental composition are observed between dendrites and inter-dendritic regions, with enrichment of Nb and Ta in the dendrites while Hf, Ti, and Zr with relatively lower melting points are more abundant in the inter-dendritic regions. The partitioning is the same as reported by Tong *et al.* [29] (and other studies [30], [60]), but the magnitude of the chemical differences is larger in the present material due to the rapid solidification associated with the gas atomization process.

5.2 X-ray scattering measurements

In view of primarily used X-ray sources, there are two categories: laboratory diffractometers and synchrotron facilities. Since the work presented in this thesis is exclusively with synchrotron radiation, all discussions of X-ray experiments throughout this thesis refer to the use of synchrotron sources. There are two reasons for the choice of synchrotron X-rays. Firstly, it is necessary to obtain high intensity for a reasonable measurement of the diffuse scattering, which is not achievable on laboratory diffractometers due to the low signal to noise ratio. Secondly, to minimize errors from Fourier transform for PDF analysis, a high $Q_{\max}$ is crucial to avoid artefacts such as termination ripples, while a too high $Q_{\max}$ can introduce noise.

Synchrotron X-rays are generated by accelerating electrons to near-light speeds and forced to travel in a curved path by a magnetic field. As the electrons travel around the storage ring, they are deflected by magnetic fields produced by insertion devices (undulators and wigglers). The change in direction causes the electrons to emit electromagnetic radiation due to the centripetal acceleration, with characteristics such as high intensity and collimation. The intensity and wavelength can be tailored by adjusting the energy of the electrons and the properties of the magnetic devices. Additionally, the high flux of synchrotron

X-rays offers a significant advantage for conducting time-resolved measurements.

(a)

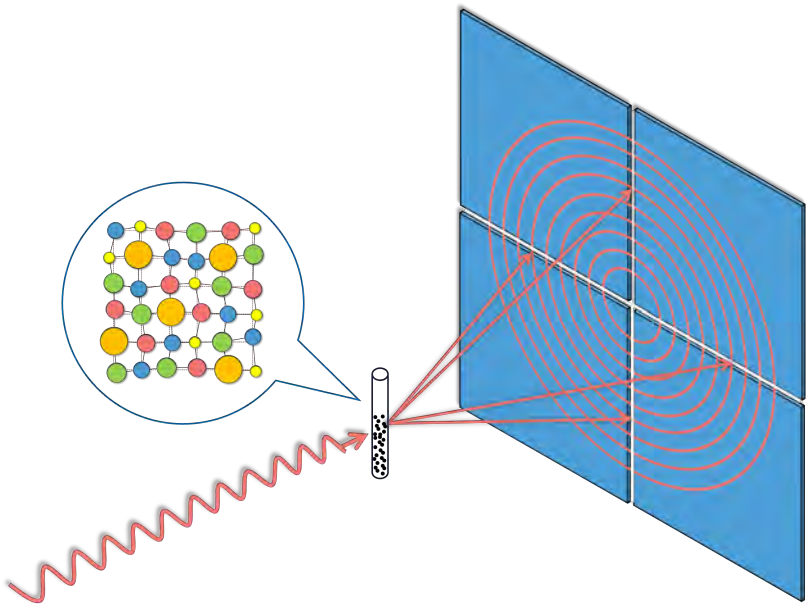

(b)

Figure 5.2: (a) Schematic illustration of a synchrotron X-ray diffraction. (b) Experimental setup of the P21.2 beamline at DESY.

In this thesis, X-ray total scattering and high-resolution diffraction experiments were performed at the P02.1 [61] and P21.2 [62] beamlines respectively, at PETRA III synchrotron (DESY, Hamburg, Germany). For the total scattering measurements, data was collected at an energy of 59.8 keV using a downstream VAREX XRD 4343CT area detector at a distance of 0.301 m. The high-resolution diffraction experiment was performed at an energy of 82 keV, with the combination of a high-resolution monochromator (a four-bounce channel-cut Si 111 producing an energy resolution of 10^{-4}) and a multi-detector setup (four VAREX XRD 4343CT detectors to cover a sufficient Q-range while maintaining a sample-to-detector distance of 2.94 m in transmission to optimize the resolution). In both experiments powder sample was contained in 1 mm quartz glass capillaries. Calibration was performed with NIST 660c LaB_6 powder, and background measurements were accounted for. Figure 5.2 (b) shows the setup of the synchrotron X-ray experiments. When the sample is irradiated by the incident X-ray beam, it scatters the X-rays producing circular rings of diffracted intensity on the 2-D detector(s). PyFAI (Python Fast Azimuthal Integration) [63] is used for the calibration and data reduction of 2-D images into 1D diffraction pattern.

5.3 Neutron scattering measurements

Similarly, because of the requirement of high energy and wide Q-range coverage (see Section 5.2), a spallation neutron source (ISIS Neutron and Muon Source, Rutherford Appleton Laboratory, UK) was chosen in this work. In a pulsed spallation source like ISIS, neutrons are produced through the collisions of accelerated protons with a heavy metal target (commonly tungsten or tantalum), and each detector measures counts as a function of time after the collision pulse. The "time-of-flight" (TOF) method is employed to determine the neutron wavelength by measuring the speed of the particle (v) according to the de Broglie relation:

$$t = \frac{L}{v} = \frac{m_{\mathrm{n}}}{h} L\lambda \tag{5.1}$$

where t is the neutron flight time from the moderator to the detector, L the distance in between, m_{n} the mass of neutron and h the Planck constant. The neutron wavelength can thus be determined directly from its flight time given known moderator-to-detector distance (L) at a specific neutron beamline.

In this thesis, neutron total scattering data was collected on the GEM diffractometer [64], [65] at ISIS. A schematic illustration of the GEM diffractometer is shown in Figure 5.3, in which a combination of several detector banks covers a scattering angle range from 1.1° to 169.3°.

At the start of each operational cycle at ISIS, calibrations are carried out to calculate the path length between the sample and detectors. Before measuring the sample, an empty run and a measurement of a vanadium can were conducted and subsequently subtracted as backgrounds, allowing for the removal of sample-unrelated effects. Using vanadium as a container material is primarily due to its negligible coherent scattering length. This makes it an

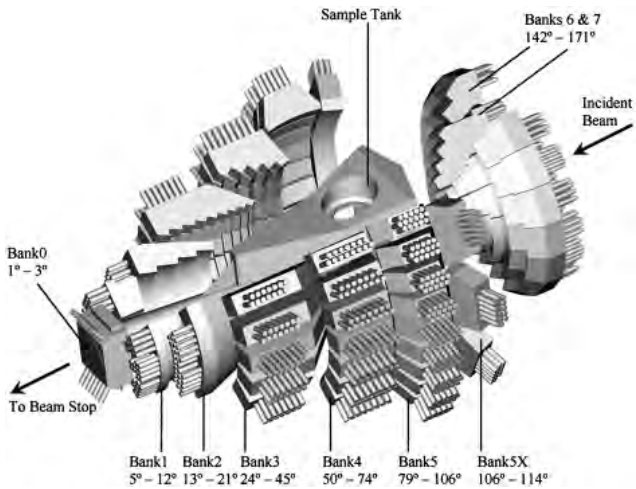

Figure 5.3: A schematic illustration of the GEM diffractometer at ISIS [64]. *Reprinted with permission from Elsevier.*

ideal material for sample cans where the aim is to measure the diffraction from the sample with minimal contribution from the container. After that, five one-hour measurements were carried out at room temperature for the HfNbTaTiZr powder mounted in a vanadium can and summed. Identical measurements were performed on pure Nb powder for reference.

5.4 Data analysis

5.4.1 Rietveld refinement

The reduced 1-D diffraction patterns are processed in GSAS-II (General Structure Analysis System) software [66], a specialized tool for crystal structure determination and diffraction-based characterization of crystalline materials. This software employs the Rietveld method [67], which is a well-established and widely acknowledged method in the field of crystallography. It utilizes the least-squares method, through adjustments to the crystal structure model to closely match the observed diffraction pattern, thus facilitating the structural refinement of diffraction data.

The diffraction data of the standard sample/calibrant (LaB_6) is refined, with the phase-related parameters (lattice parameters, site occupancies, atomic positions and atomic displacement parameters etc.) fixed, while the background, arbitrary scaling factor and instrument parameters being refined. As the standards have known lattice parameters, and are confirmed to have no strain or size-related broadening, it is possible to isolate the instrumental contribution. An instrument parameter file is generated to be used in refinements of samples. This step is to exclude sample-unrelated effects.

In the subsequent refinement process of samples, the instrument parameters

remained fixed, while sample-related parameters are refined. Here, lattice parameter a, isotropic atomic displacements parameter U_{iso}, and microstrain were refined. U_{iso} was constrained to be the same for all atoms within the BCC structure (space group $\text{I}m\bar{3}m$). The unit's site occupancy was based on the alloy's average composition from the EDS analysis (see Table 5.1). Microstrain was refined to obtain good fits, accounting for the potential high dislocation density from the as-atomised sample, and the broad distribution of lattice parameters originating from the varying chemistry across dendrites and inter-dendritic regions (Figure 5.1). With a and U_{iso} being extracted, LLDs were able to be calculated from Eq. 3.2, (3.4) and (3.11), reducing to

$$\varepsilon_{\text{s}} = \frac{\sqrt{U_{\text{iso}} - U_{\text{t}}}}{\frac{\sqrt{3}}{4}a}, \tag{5.2}$$

where the method of determining thermal component of the displacement parameter U_{t} was generally discussed in Section 3.3.2, and details shown in Section 6.1.

5.4.2 Small-box analysis

For X-ray total scattering, the calibration and reduction were performed similarly as illustrated in Section 5.2. The data was then transformed to PDF using PDFgetX3 [68] with $Q_{\text{max}} = 21.04$ Å^{-1}. The raw neutron total scattering data was processed using the GudrunN software, specifically developed at ISIS for analyzing total scattering data from spallation sources [69]. This software requires datasets of background, sample containers (e.g., vanadium can in this case), and any relevant sample environment (such as furnaces or cryostats). It normalises these inputs and subtracts them from the raw experimental data to isolate the scattering attributable to the sample itself. The resultant data was then Fourier transformed into PDFs with $Q_{\text{max}} = 34$ Å^{-1}. Subsequent analyses were performed in the PDFgui software.

Small-box analysis of the PDFs was performed in the PDFgui software [58], [59]. As mentioned earlier in Section 4.2.5.2, atomic displacements lead to peak broadening in the PDF. In the PDFgui software, the peak width (σ) is modelled as Eq. 4.20. While a, U_{iso} and δ_2 were refined, the value of Q_{broad} and Q_{damp} (which describes the dampening of the PDF peak in real-space due to instrument resolution) were determined by fitting the PDF from the reference (LaB_6 in the case of X-rays and Nb in the case of neutrons). The PDFs were fitted in the range $r \leq 20$ Å, as this range is relatively robust to artifacts induced by instrumental resolution [70]. According to Eq. 5.2, LLDs were calculated.

Chapter 6

Results and discussion

6.1 Separation of thermal components

Identifying LLDs, or static displacements, presents a significant challenge due to their convolution with atomic thermal vibrations, as mentioned in Section 3.3.2. To accurately extract LLDs it is essential to separate the static contributions from the thermal components (see Eq. 3.11). An experimental methodology for achieving this separation involves conducting temperature-dependent scattering experiments at cryogenic temperatures. At such low temperatures, the B-factor (see Eq. 4.18) only depends on the mass M of the atoms and the Debye temperature of the material θ_D [33]:

$$B \to \frac{6\pi^2\hbar^2}{Mk\theta_D} \tag{6.1}$$

where the Debye temperature θ_D can be fitted through variable temperature measurements. With θ_D and M known, B at 0 K can be calculated and the thermal components of the atomic displacements at any temperatures can be determined [33]. However, conducting in situ scattering experiments at cryogenic temperatures may not always be experimentally viable e.g., in the case of in situ high-temperature measurements or when comparing multiple alloys, as such experiments are time-consuming. In these instances, it becomes necessary to make approximate estimations of the thermal contribution.

In this thesis, a methodology for estimating the thermal displacements in RHEAs is proposed, applying the rule-of-mixtures (ROM). This approach calculates the thermal components U_t by considering the individual displacement parameters of single components within an alloy at the same temperature, as shown in:

$$U_\mathrm{t}^T = \sum_i c_i U_i^T \tag{6.2}$$

where c_i is the concentration and U_i^T the displacement parameter of element i (in an alloy) at temperature T.

Note that two terms need to be determined here, the elemental displacement parameters U_i^T and the temperature T at which the displacement parameters

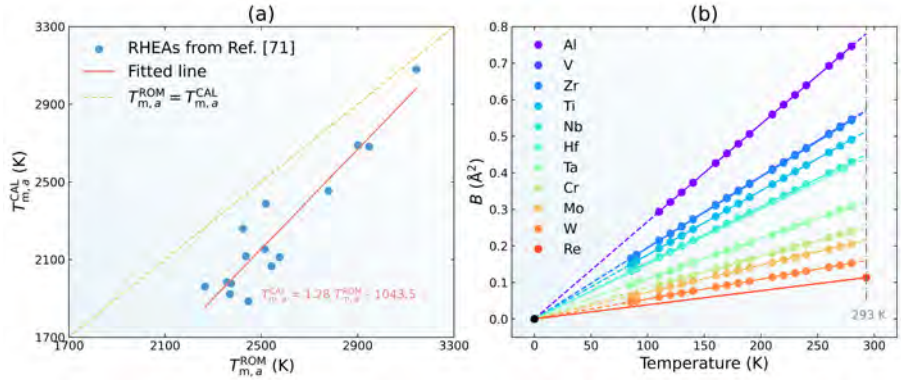

Figure 6.1: (a) The linear relationship between $T^{\mathrm{ROM}}_{\mathrm{m},a}$ and $T^{\mathrm{CAL}}_{\mathrm{m},a}$. The blue points are the alloys investigated in Ref. [71] involving the same elements as in Ref. [29]. (b) Linear fit of B-factors. Values denoted as circle derived from Ref. [72]–[74]. Note here data skipped/lacked in low temperature region is deemed less critical for this analysis, as the focus is primarily on data around room temperature.

are calculated. It has been proposed by Owen et al. [33] that the U_i^T values are considered at a uniform homologous temperature ($\tau = T/T_m$) to account for the effects of thermal vibrations on bond strength and, consequently, the melting temperature of the alloy [32]. To determine the homologous temperature, the melting temperature of the alloy, $T_{\mathrm{m},a}$, must be known. This is often not available and must also be estimated from the corresponding values of the individual components. Based on this, two methods were proposed to calculate the temperature:

- ROM method: This method applies ROM to calculate the melting temperature of the alloy ($T^{\mathrm{ROM}}_{\mathrm{m},a}$).
- CALPHAD adjusted method: This method adjusts the $T^{\mathrm{ROM}}_{\mathrm{m},a}$ by performing a first-order correction based on CALPHAD (CALculation of PHAse Diagrams) calculations, as demonstrated by Senkov et al. [71].

The correction is shown in Figure 6.1. Further elaboration on these methods, including their mathematical expression is provided in Paper I.

The other term, the elemental displacement parameters U_i^T are calculated from temperature-dependent B-factors for each element using the formula:

$$U_i^T = \frac{B_i^T}{8\pi^2}, \tag{6.3}$$

where B_i^T is the B-factor of element i at temperature T, which are derived from the linear inter- and extrapolation of the values reported in Ref. [72]–[74], as shown in Figure 6.1. More detailed calculation results can be found in the supplementary material of Paper I.

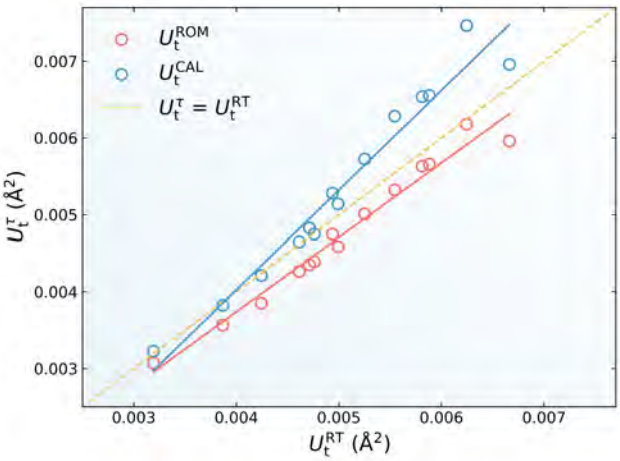

Figure 6.2: Comparison between different methods of evaluating thermal components of U_{iso} from various RHEAs. The solid lines are linear fits for respective methods.

With both temperature and elemental displacement parameters determined, the subsequent thermal components of the displacement parameters U_{t}^{T} can be calculated using Eq. 6.2, includes $U_{\mathrm{t}}^{\mathrm{ROM}}$ and $U_{\mathrm{t}}^{\mathrm{CAL}}$ based on the two methods for determining the homologous temperature (denoted as τ). Additionally, $U_{\mathrm{t}}^{\mathrm{RT}}$ was calculated using room temperature B-values for all elements for comparison. Detailed calculation results can be found in the supplementary material of Paper I. Figure 6.2 shows a comparison of the different approaches, where the overall differences are minor in spite of increasing discrepancies observed at high U_{t} values.

In this part, different assumptions were made for the separation of thermal contributions of atomic displacements. The estimations presented here provide a relatively robust and practical methodology for isolating static displacements. This is promising for future studies, as it suggests that U_{iso}-based analysis without variable-temperature (cryogenic) measurements offers a sufficiently accurate way to measure the thermal components and subsequently, the LLDs.

6.2 Quantification of LLDs in RHEAs

By applying the methodology outlined in Section 3.3, it is possible to quantify LLDs once the thermal components have been determined, as established in Section 6.1. This approach was applied to quantify LLDs in RHEAs that Tong et al. reported in Ref. [29], with thermal contributions separated. Furthermore, one prototype material (gas atomised equiatomic HfNbTaTiZr) was examined through both real-space and reciprocal-space refinements of synchrotron X-ray data, complemented by a comparison with a real-space analysis of neutron total scattering data for the same alloy. Results indicate pronounced LLDs

Table 6.1: Values of LLDs (ε_s), displacement parameters (U_{iso}), lattice parameters (a), thermal (U_t^{CAL}) and static (U_s) components of the displacements for RHEAs studied in Ref. [29].

Composition	ε_s (%)	U_{iso}† (Å^2)	U_t^{CAL*} (Å^2)	U_s* (Å^2)	a† (Å)
HfNbTaTiZr	10.18	0.0291	0.0065	0.0226	3.4088
HfNbTiZr	9.91	0.0292	0.0075	0.0217	3.4359
NbTiVZr	10.61	0.0302	0.0070	0.0232	3.3181
MoNbReTaTiVW	4.66	0.0083	0.0042	0.0041	3.1678
MoNbReTaVW	4.54	0.0077	0.0038	0.0039	3.1653
MoNbTaTiVW	5.50	0.0106	0.0048	0.0058	3.1911
MoNbReTaW	4.08	0.0064	0.0032	0.0032	3.1901
MoNbTaTiV	6.85	0.0148	0.0057	0.0091	3.2119
NbReTaTiV	6.67	0.0136	0.0051	0.0085	3.1865
MoNbTaV	6.18	0.0126	0.0053	0.0073	3.1998
MoNbTiV	6.53	0.0144	0.0063	0.0081	3.1846
NbReTaV	5.80	0.0110	0.0046	0.0064	3.1750
NbTaTiV	6.57	0.0150	0.0066	0.0084	3.2319
NbTaVW	6.39	0.0126	0.0047	0.0079	3.2043
Nb	0	0.0060	-	0	3.2980

† From Ref. [29].
* From Paper I.

in the analysed BCC-structured RHEAs, and confirm the consistency and reliability of the scattering-based techniques in probing LLDs by showing a decent agreement on the outcomes.

6.2.1 LLDs of RHEAs from literature

According to Eq. 5.2, U_{iso}, U_t and a are required to calculate the values of LLDs. Using the U_{iso} and a reported in Ref. [29], along with the calculated thermal components U_t detailed in Paper I, LLDs of these RHEAs are calculated and results are listed in Table 6.1. Note that the reason for choosing U_t^{CAL} is because it provides the most conservative estimation of the static contributions, i.e., the smallest LLDs.

The results presented in Table 6.1 show that there appears to be a correlation between the chemical composition and ε_s. Notably, the first three RHEAs,

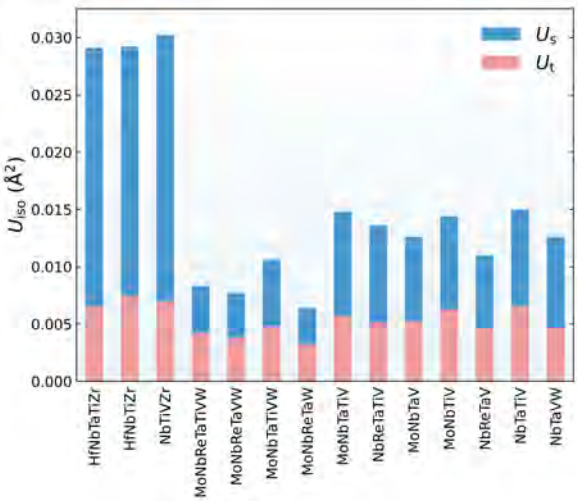

Figure 6.3: Static (U_s) and thermal (U_t) component of the off-site displacements (U_{iso}) extracted from several RHEAs [29]. Thermal displacements calculated from a linear extrapolation model (described in section 6.1) and total U_{iso} determined experimentally by Tong et al. [29] from diffraction data. The relatively larger magnitude of U_s than U_t indicates that LLDs in BCC-structured RHEAs are severe.

all of which containing Zr, exhibit significantly large LLD (ε_s) values around 10%. This differs from the remaining RHEAs, where the average ε_s value is around 5.85 ± 1.0 % with small variations among them. It is observed that the addition or removal of Hf and Zr is expected to significantly affect LLDs, which might be due to the extensive charge transfer and associated change in effective size [29], [75], [76].

The magnitude of the static and thermal components of the off-site displacements in RHEAs are visually illustrated in Figure 6.3. Notably, the static displacements are shown to be of comparable level to or even surpassing that of the thermal displacements. This is in contrast to the case of FCC-structured HEAs, where the thermal displacements are considerably larger than the static displacements [33]. Such a comparison clearly shows the significant presence of LLDs within BCC-structured RHEAs.

6.2.2 LLDs of a HfNbTaTiZr RHEA

Similar to Section 6.2.1, LLDs of a HfNbTaTiZr RHEA were quantified using Eq. 5.2, with lattice parameter a and displacement parameter U_{iso} obtained from refinements of scattering experiment data, and $U_t = 0.0065$ Å^2. The results are shown in Table 6.2. The comparison between different analytical methods, i.e., diffraction and PDF, as well as radiation type (X-ray and neutron), reveals a notable consistency in lattice parameters and LLDs. Such a nice agreement supports the reliability and robustness of these techniques and sources in

Table 6.2: Comparison of lattice parameters (a), off-site displacement parameters (U_{iso}), and local lattice strain (ε_{s}) for the HfNbTaTiZr RHEA from reciprocal-space and real-space (PDF) analysis of synchrotron and neutron data.

	X-ray		**Neutron**
	Diffraction	PDF	PDF
a (Å)	3.4019(1)	3.4010(8)	3.4041(6)
U_{iso} (Å^2)	0.0158(2)	0.0197(6)	0.0168(4)
ε_{s} (%)	6.53	7.76	7.16

accurately quantifying LLDs. It is noted that the LLD value derived from X-ray diffraction refinement is 6.53 %, which is significantly smaller than the value obtained from U_{iso} reported by Tong et al. [29] (10.18 %, see Table 6.1). Without comprehensive data on other alloys, it is uncertain whether this difference represents a systematic variation across different RHEAs, or if it is a phenomenon unique to the HfNbTaTiZr RHEA. Further investigation and data collection on a broader range of RHEAs are required to clarify this discrepancy.

The X-ray diffractogram and the result of the Rietveld refinement are shown in Figure 6.4, in which a significant decay with increasing Q can be observed, due to the combined effects of LLDs, thermal vibrations and X-ray form factor as previously discussed in Section 4.2.5.1. Furthermore, the fitting of PDFs

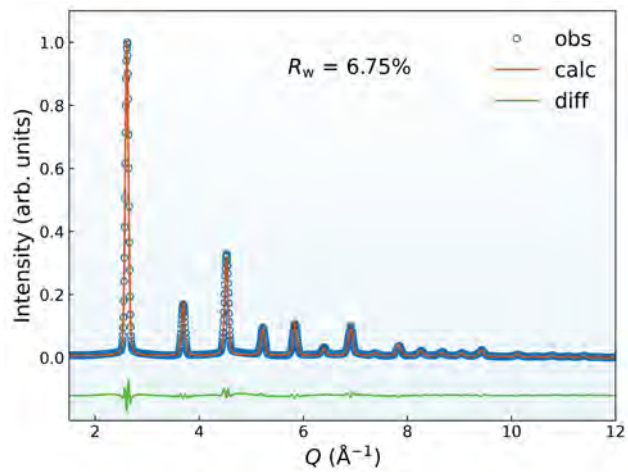

Figure 6.4: The X-ray diffractogram, including results from Rietveld refinement of HfNbTaTiZr. R_{w} is the overall weighted profile R-factor as a statistical measure to quantify the difference between the observed and calculated X-ray diffraction patterns.

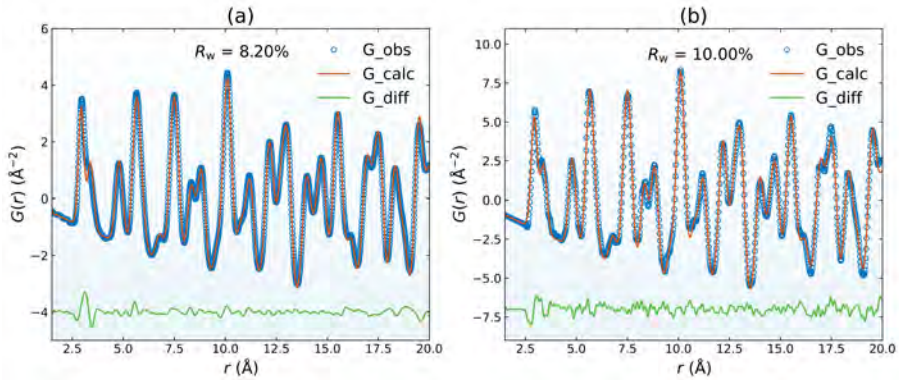

Figure 6.5: (a) The X-ray and (b) neutron PDF including small-box fitting results of HfNbTaTiZr.

shown in Figure 6.5 reveals overall good fit although there are deviations at the first-nearest-neighbor (1NN) and the second-nearest-neighbor (2NN) due to the weighting effect. The PDFs are weighted by partial atomic pairs, with each contributing to the overall peak, as can be seen from DFT calculations [29].

In this part, LLDs for a range of RHEAs from Ref. [29] were quantified. The results show that LLDs are pronounced within BCC-structured RHEAs compared to their FCC-structured counterparts. Further analysis of a HfNbTaTiZr RHEA has shown a good agreement between real-space (PDF) and reciprocal-space (diffraction) results of X-ray scattering data. Additionally, consistent results between neutron and X-ray PDF analyses indicate that the radiation type has a negligible impact.

6.3 The effects of segregation on the determination of LLDs

Quantification of LLDs using single-phase small-box modelling assumes the material studied to be homogeneous, i.e., free of inhomogeneities such as preferred orientation, microstrain, or nonuniform crystallite size. However, this is not always the case in practice, as demonstrated by the dendritic microstructures observed in the HfNbTaTiZr RHEA shown in Figure 5.1. This characteristic has also been noted in various as-cast RHEAs as shown in Figure 2.3 and literature [17], [77]–[79]. Such dendritic microstructures derive from the alloys' compositional complexity and the varying melting temperatures of their constituent elements [23]. This observation raises a critical question about the potential impact of chemical segregation on the validity of the small-box analysis. To address this question, a comprehensive simulation study was undertaken. Synthetic PDFs were generated to simulate the segregated microstructures of the HfNbTaTiZr RHEA and subsequently fitted with a

Table 6.3: Elemental neutron scattering lengths (b) [80] and calculated average values for dendrites (D) and inter-dendritic regions (ID) based on their chemistry from Table 5.1.

	Element					**D**	**ID**
	Hf	Nb	Ta	Ti	Zr		
b (fm)	7.70	7.05	6.91	-3.44	7.16	5.24	4.31

single-phase model. This approach was later extended to a wider range of RHEAs, aiming for a broader understanding of how chemical segregation affects the accuracy of LLD determination. The simulation and fitting were done using the DiffPy-CMI modeling framework [59].

6.3.1 Quantifying LLD errors in HfNbTaTiZr

A segregated microstructure is characterised by continuous modulations in its chemical composition. For simplicity, this structure can be viewed as comprising two distinct phases: dendrites (D) and inter-dendritic regions (ID). Each phase has a different chemical composition and, as a result, distinct lattice parameter. Following the methodology proposed by Sawinski [81], the overall PDF of such a multiphase system can be mathematically represented as a weighted sum of the individual PDFs of each phase:

$$G(r) = \sum_p \frac{x_p \bar{b}_p^2}{\sum_p x_p \bar{b}_p^2} G_p(r) \tag{6.4}$$

where x_p is the molar fraction, $\bar{b}_p$ the average scattering length, and $G_p(r)$ the PDF with the subscript p indicating the phase. Particularly, $\bar{b}_p$ could be

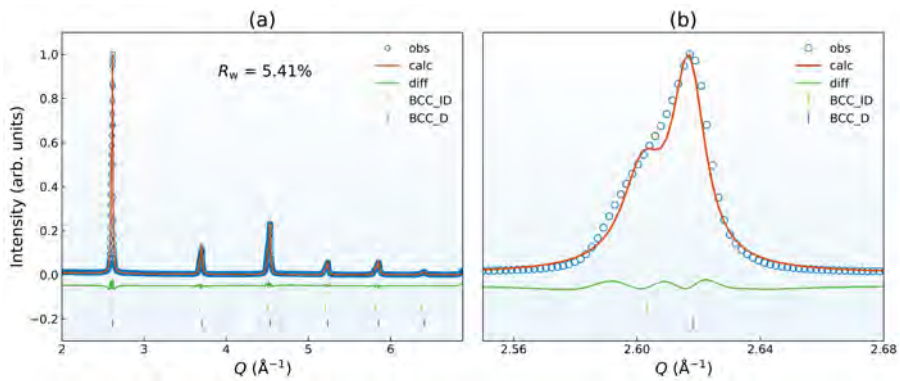

Figure 6.6: (a) The high-resolution X-ray diffractogram, including results from the two-phase Rietveld refinement of HfNbTaTiZr. (b) Magnified view of the 110 peak.

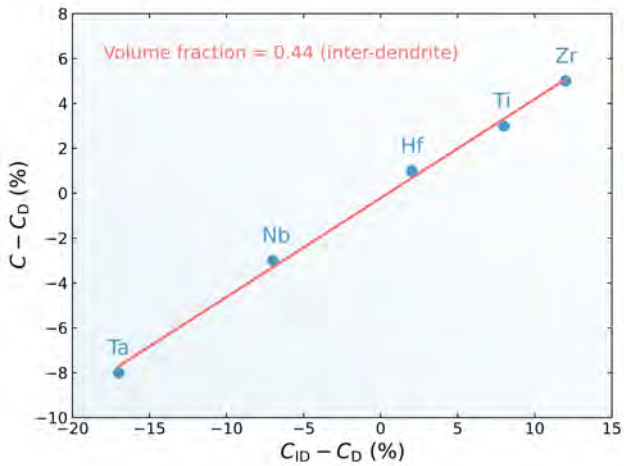

Figure 6.7: The volume fraction of inter-dendritic region estimated by lever rule from chemical compositions in Table 5.1. Volume fraction $V_F = \frac{C-C_D}{C_{ID}-C_D}$, where C is the bulk concentration of one element, C_D the concentration of the element in dendrite, C_{ID} the concentration of the element in inter-dendritic region.

calculated based on the chemical composition of dendrites and inter-dendritic regions ($\bar{b}_p = \sum_i c_{i,p} b_{i,p}$) as shown in Table 6.3. Additionally, when the difference in lattice parameters between the "two phases" is small, volume fractions may be used as a substitute for molar fractions.

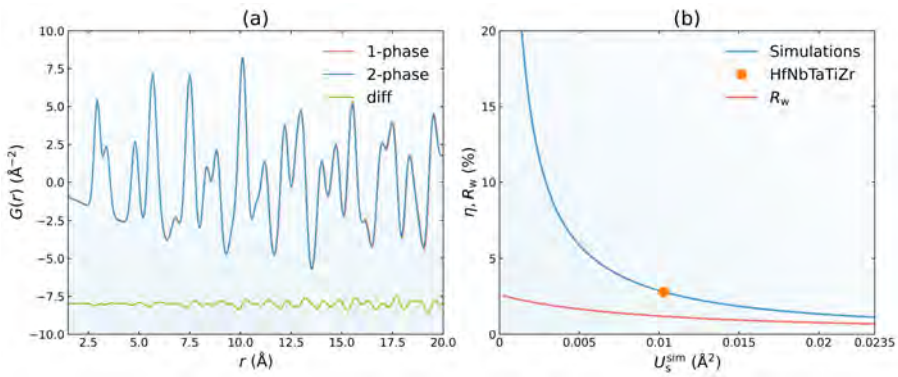

Figure 6.8: (a) Comparison of simulated PDFs for the HfNbTaTiZr alloy in homogeneous (1-phase) and segregated (2-phase) microstructures. (b) The error distribution of LLDs from single-phase PDF analysis of simulated PDFs, with respect to the magnitude of LLDs (U_s^{sim}). The orange point denotes the HfNbTaTiZr alloy applying the U_{iso} value from neutron PDF data. R_w is the weighted profile R-factor from the fits.

To simulate PDFs, essential parameters such as lattice parameters and volume fractions are required. These parameters are obtained from the Rietveld refinement of high-resolution synchrotron X-ray diffraction data, as shown in Figure 6.6. The segregation could be clearly seen from the slightly asymmetric 110 peaks in Figure 6.6 (b).The refinement gives results: $a_{\mathrm{D}} = 3.3938(1)$ Å (the lattice parameter of dendrites), $a_{\mathrm{ID}} = 3.4129(2)$ Å (the lattice parameter of inter-dendritic regions), and the volume fraction $V_{\mathrm{F}} = 0.47(1)$, which is in good agreement with the value obtained from the partitioning of alloying elements, 0.44 (See Figure 6.7).

A theoretical two-phase PDF was generated using the lattice parameters for both phases. Identical isotropic displacement parameters (U_{iso}) for both phases were employed (from the neutron data analysis see Table 6.2). The instrumental effect was accounted for by applying instrument-related parameters from fitting the neutron PDF of Nb (detailed in Paper I). The two-phase PDF was then compared with a single-phase PDF ($a = 3.4041$ Å from Table 6.2) as shown in Figure 6.8 (a), where only minor differences can be observed, indicating that chemical segregation has a negligible impact on the PDF of HfNbTaTiZr. To further explore the effect of segregation on determining LLDs, a series of 100 two-phase PDFs with variable U_{iso} values were simulated and fitted with a single-phase model to assess the relative error (η) between the fits and the simulated data (more details in Paper I). The results are shown in Figure 6.8 (b), where an inverse correlation between $U_{\mathrm{s}}^{\mathrm{sim}}$ (the simulated static U_{iso} value) and η is seen. Notably, a rapid increase in error is observed at lower $U_{\mathrm{s}}^{\mathrm{sim}}$ values, where care must be taken. But for the HfNbTaTiZr RHEA (depicted as an orange point in Figure 6.8 (b)), the error is around 3%, which is acceptable and should not be a problem on the determination of the LLD. On the other hand, the R_{w} values which reveals the fitting quality do not show significant increase

Table 6.4: Reported lattice parameters and their differences in some segregated BCC-structured HEAs.

Alloy	a_1 (Å)	a_2 (Å)	Δa (%)	Ref.
HfNbTaTiZr	3.397	3.4181	0.62	[30]
HfNbTaTiZrW	3.286	3.376	2.74	[79]
HfNbTaTiZrMoW	3.273	3.348	2.29	[79]
WMoCrTiAl	3.178	3.154	0.76	[78]
TiNbTaZrMo	3.25	3.33	2.46	[82]
$(TiVCr)_{95}W_5$	3.072	3.105	1.07	[83]
MoVW	3.11	3.05	1.93	[84]
CrMoVW	3.077	3.008	2.24	[84]
$V_{2.5}Cr_{1.2}WMoCo_{0.04}$	3.0594	3.1603	3.30	[85]

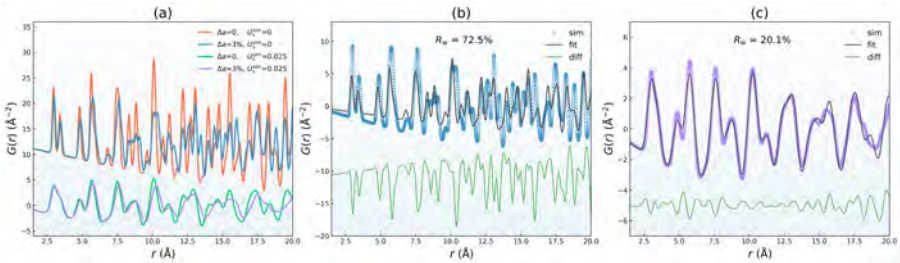

Figure 6.9: (a) Extreme cases of simulated composite PDFs with $x_{\mathrm{ID}} = 0.5$. (b) and (c) Single-phase fits to the PDFs corresponding to $\Delta a = 3\%/U_{\mathrm{s}}^{\mathrm{sim}} = 0$ and corresponding to $\Delta a = 3\%/U_{\mathrm{s}}^{\mathrm{sim}} = 0.025$, respectively. R_{w} is the weighted profile R-factor from the fits.

at decreasing $U_{\mathrm{s}}^{\mathrm{sim}}$, probably due to the small lattice parameter difference between the two phases (3.3938 and 3.4129 Å respectively correspinding to 0.56 %).

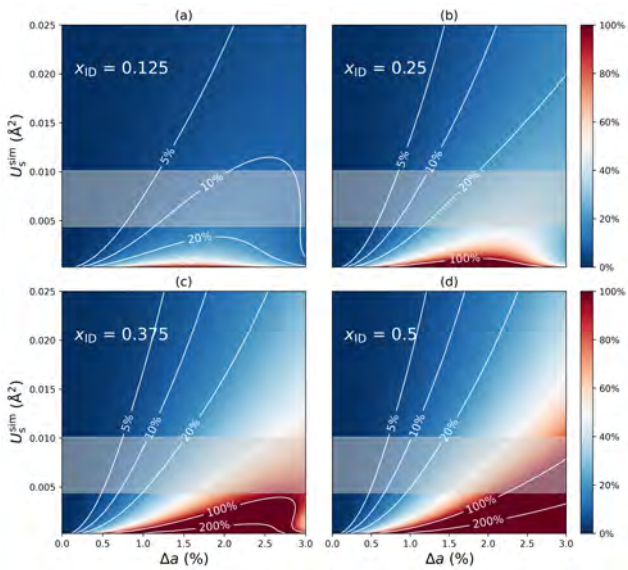

Figure 6.10: The distribution of the error (η) of LLDs. Each pixel point corresponds to a value of the difference between LLDs from simulated and fitted PDFs. The color scale indicates the magnitude of the error, with red indicating great errors while blue indicates small errors. The contour lines represent the error with the same value. The translucent regions show the typical U_{s} range in RHEAs, as determined in Paper I.

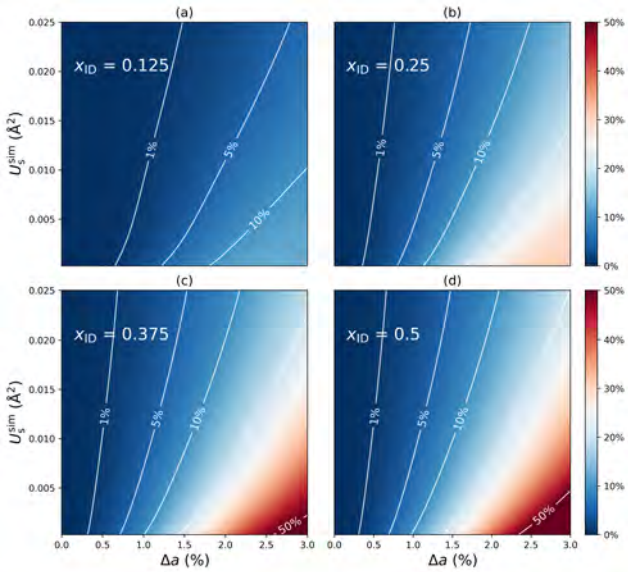

Figure 6.11: The distribution of the R_w values. Each pixel point corresponds to a value of the R_w which is an indicator of the fitting quality. The color scale indicates its magnitude, with red indicating great values while blue indicates small values. The contour lines represent the same R_w value.

6.3.2 Quantifying LLD errors in RHEAs

While the analysis indicates that the effect of segregation on the determination of LLDs in the HfNbTaTiZr alloy is marginal, this conclusion is limited to this specific alloy. To extend the understanding of how segregation influences LLD errors more broadly across different alloys, a comprehensive simulation study involving a variety of BCC-structured HEAs was performed. This study allows for an assessment of both the degree of chemical segregation and the extent of LLDs. Additionally, the study explored how differences in scattering lengths between dendritic and inter-dendritic regions could affect the accuracy of LLD quantification.

Similar simulations and fittings as described in Section 6.3.1 were performed (more details can be found in Paper II). Firstly, the impact of variation in lattice parameters and molar fractions on the accuracy of LLDs measurements was investigated. Specifically, a maximum difference in lattice parameters of the two phases was set to be 3 % based on reported lattice parameters difference in the literature, see Table 6.4. For each specified difference in lattice parameters ($\Delta a = |a_2 - a_1|/a_1$), the static displacement parameters U_s^{sim} were varied from 0 to 0.025 Å^2. Moreover, the molar fractions x_{ID} were changed in steps (0.125, 0.25, 0.375, 0.5).

Figure 6.9 (a) shows the resulting two-phase PDFs corresponding to the extreme cases for $x_{ID} = 0.5$. In scenarios where significant LLDs are present, characterised by a high value of U_s^{sim}, the influence of segregation on the PDF

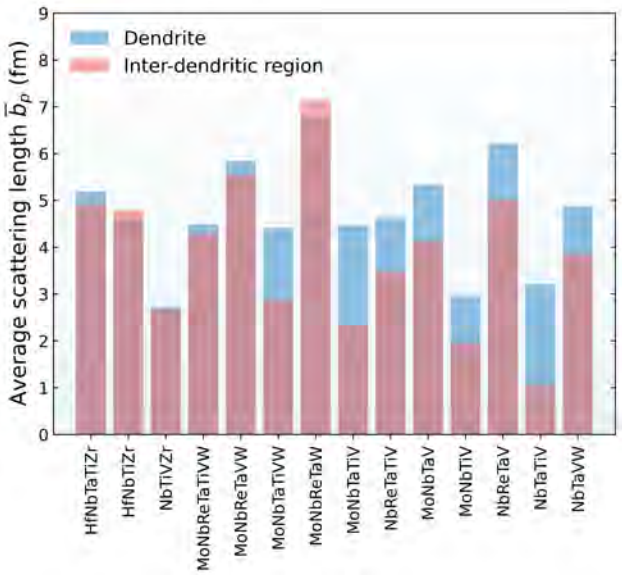

Figure 6.12: The average scattering lengths of dendrites and inter-dendritic regions from alloys in Ref. [29].

is found to be relatively minor (the green and purple curves). Conversely, in cases where LLDs are absent ($U_{\mathrm{s}}^{\mathrm{sim}} = 0$), the segregation effect becomes much more pronounced, leading to noticeable discrepancies in the PDFs (the red and blue curves). Fitting composite PDFs, particularly those with large lattice parameter differences, to a single-phase model leads to significant deviations from the model, as shown in Figure 6.9(b) and (c).

The error, η, is plotted as a function of Δa and $U_{\mathrm{s}}^{\mathrm{sim}}$ for each molar fraction in Figure 6.10, with the red regions as an indicator of the greater errors i.e., problematic cases. It is noted that the distribution of the error does not follow a monotone increasing tendency, but an unexpected decrease occurs at a certain point. This is due to the poor fitting quality at regions with low $U_{\mathrm{s}}^{\mathrm{sim}}$ and large Δa values (see Figure 6.11). Even if the error appears to decrease at some point, it may simply be a random effect, rather than indicating increased reliability or physical meaningfulness in the results, one example is observed in Figure 6.9 (b), where a exceedingly large R_{w} value of 72.5 % suggests the derived parameters may not possess physical meaning.

A reasonably accurate estimate for the investigated RHEAs (translucent region in Figure 6.10) seems to be at $\Delta a \lesssim 1\%$, where both η and R_{w} present relatively low values. But only a few HEAs from Table 6.4 fulfill this, and for most RHEAs (e.g., from Table 6.1) the lattice parameter difference Δa is unknown. To draw further conclusion, high-resolution diffraction experiments are needed to determine Δa for RHEAs. It should also be noted that this is rather an idealised case as here all instrumental parameters are known, which is not the case in reality.

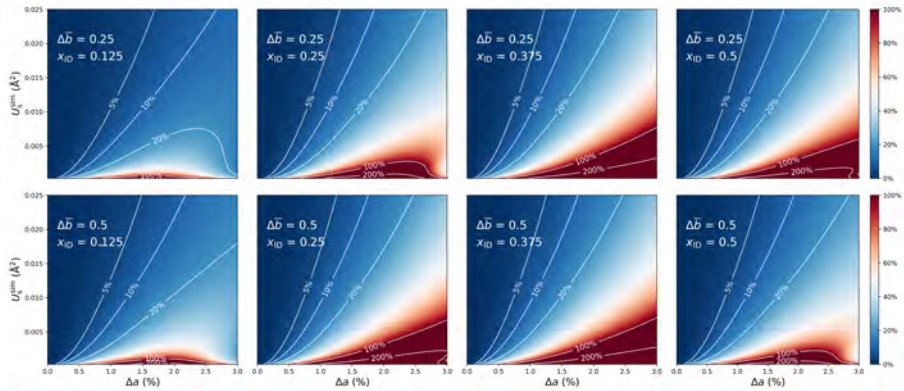

Figure 6.13: Visualisation of the impact of average scattering length differences and molar fraction on error determination.

In the previous simulations, the scattering lengths for the "two phases" within the RHEAs were simplified to be identical. However, RHEAs can exhibit relatively large differences in average scattering lengths between dendrites and inter-dendritic regions as shown in Figure 6.12 (e.g., NbTaTiV and MoNbTaTiV). To investigate the effect of average scattering length difference on LLD errors, similar simulations were performed as earlier, but specifically with average scattering lengths difference of 25 % ($\Delta\bar{b} = (\bar{b}_2 - \bar{b}_1)/\bar{b}_1 = 0.25$) and 50 % ($\Delta\bar{b} = 0.5$). The resulting error is plotted in Figure 6.13. The effect of the scattering length difference is relatively small compared with Figure 6.10.

In this section, composite PDFs were simulated for a HfNbTaTiZr RHEA and other segregated RHEAs to explore the validity of using single-phase model for the LLD determination. It reveals that the effect of segregation is negligible for the HfNbTaTiZr RHEA, while in general cases, significant inaccuracies could arise under certain conditions, with the errors being dependent on both the extent of segregation and the magnitude of LLDs. Moreover, the simulations suggest that the impact of scattering length differences plays a minor role in the determination of LLDs.

6.4 Conclusions and Outlook

In this thesis, LLDs in RHEAs were quantified using scattering experiments and simulations. Based on the results, the following conclusions can be drawn:

- Small-box PDF analysis is generally a reliable tool for quantifying LLDs, and LLDs are measured to be severe in BCC-structured RHEAs.

- The process of determining LLDs in the chemically segregated HfNbTaTiZr RHEA through fitting with a single-phase model in PDF analysis revealed that the associated error is negligible.

- A comprehensive simulation study across a broad range of RHEAs revealed that segregation can significantly affect the accuracy of LLD determinations in certain scenarios. Specifically, when the lattice parameters difference between the segregated regions is large, the errors in LLD measurements become pronounced.

Based on the findings and discussions presented, several avenues for future work emerge:

- The experimental work focused only on the HfNbTaTiZr RHEA. Investigating a wider range of RHEAs is crucial to determine if the conclusions drawn are consistent or are specific to the studied alloy.

- The observed errors in determining LLDs were especially significant in BCC-structured RHEAs that exhibited considerable lattice parameter differences. In contrast, FCC-structured RHEAs typically show smaller variations in lattice parameters, which suggests that the methodologies applied in this study might be more effective when applied to FCC-structured RHEAs.

- The segregated microstructures pose challenges to small-box PDF analysis in certain scenarios. Determining U_{iso} from reciprocal-space refinements is a potentially more suitable approach in cases of pronounced segregation. A similar simulation study on reciprocal space-based LLD characterisation in segregated structure would be interesting.

Bibliography

[1] I. Mazínová and P. Florian, *Materials selection in mechanical design*. Elsevier, 2014, vol. 16, pp. 145–153, ISBN: 9781856176637.

[2] R. C. Reed, *The Superalloys fundamentals and applications*. Cambridge University Press, Sep. 2006, vol. 9780521859, pp. 1–372, ISBN: 9780511541285.

[3] M. J. Donachie and S. J. Donachie, *Superalloys*. ASM International, Mar. 2002, ISBN: 978-1-62708-267-9.

[4] C. W. Weyhrich, S. P. Petrova, K. J. Edgar and T. E. Long, "Renewed interest in biopolymer composites: incorporation of renewable, plant-sourced fibers," *Green Chemistry*, 25 (1), 106–129, 2022,

[5] J. W. Yeh, S. K. Chen, S. J. Lin *et al.*, "Nanostructured high-entropy alloys with multiple principal elements: Novel alloy design concepts and outcomes," *Advanced Engineering Materials*, 6 (5), 299–303, 2004,

[6] B. Cantor, I. T. Chang, P. Knight and A. J. Vincent, "Microstructural development in equiatomic multicomponent alloys," *Materials Science and Engineering: A*, 375-377 (1-2 SPEC. ISS.), 213–218, Jul. 2004,

[7] E. P. George, D. Raabe and R. O. Ritchie, "High-entropy alloys," *Nature Reviews Materials*, 4 (8), 515–534, 2019,

[8] D. B. Miracle and O. N. Senkov, "A critical review of high entropy alloys and related concepts," *Acta Materialia*, 122, 448–511, 2017,

[9] O. N. Senkov, G. B. Wilks, J. M. Scott and D. B. Miracle, "Mechanical properties of Nb25Mo25Ta 25W25 and V20Nb20Mo 20Ta20W20 refractory high entropy alloys," *Intermetallics*, 19 (5), 698–706, 2011,

[10] Z. Wang, Q. Fang, J. Li, B. Liu and Y. Liu, "Effect of lattice distortion on solid solution strengthening of BCC high-entropy alloys," *Journal of Materials Science and Technology*, 34 (2), 349–354, 2018,

[11] P. Thirathipviwat, S. Sato, G. Song *et al.*, "A role of atomic size misfit in lattice distortion and solid solution strengthening of TiNbHfTaZr high entropy alloy system," *Scripta Materialia*, 210, 114470, 2022,

[12] Y. Y. Zhao, Z. F. Lei, Z. P. Lu, J. C. Huang and T. G. Nieh, "A simplified model connecting lattice distortion with friction stress of nb-based equiatomic high-entropy alloys," *Materials Research Letters*, 7 (8), 340–346, 2019,

[13] C. Lee, Y. Chou, G. Kim *et al.*, "Lattice-Distortion-Enhanced Yield Strength in a Refractory High-Entropy Alloy," *Advanced Materials*, 32 (49), 2004029, 2020,

[14] J. W. Yeh, "Recent progress in high-entropy alloys," *Annales de Chimie: Science des Materiaux*, 31 (6), 633–648, 2006,

[15] O. N. Senkov, J. M. Scott, S. V. Senkova, F. Meisenkothen, D. B. Miracle and C. F. Woodward, "Microstructure and elevated temperature properties of a refractory TaNbHfZrTi alloy," *Journal of Materials Science*, 47 (9), 4062–4074, 2012,

[16] O. N. Senkov, J. M. Scott, S. V. Senkova, D. B. Miracle and C. F. Woodward, "Microstructure and room temperature properties of a high-entropy TaNbHfZrTi alloy," *Journal of Alloys and Compounds*, 509 (20), 6043–6048, 2011,

[17] O. N. Senkov, G. B. Wilks, D. B. Miracle, C. P. Chuang and P. K. Liaw, "Refractory high-entropy alloys," *Intermetallics*, 18 (9), 1758–1765, 2010,

[18] W. Benenson, J. W. Harris, H. Stocker and H. Lutz, *Handbook of Physics*. New York, NY: Springer New York, 2002, pp. 1–1185, ISBN: 978-0-387-95269-7.

[19] D. B. Miracle, M. H. Tsai, O. N. Senkov, V. Soni and R. Banerjee, "Refractory high entropy superalloys (RSAs)," *Scripta Materialia*, 187, 445–452, 2020,

[20] Z. D. Han, H. W. Luan, X. Liu *et al.*, "Microstructures and mechanical properties of TixNbMoTaW refractory high-entropy alloys," *Materials Science and Engineering: A*, 712 (December 2017), 380–385, 2018,

[21] E. Fazakas, V. Zadorozhnyy, L. K. Varga *et al.*, "Experimental and theoretical study of Ti20Zr20Hf 20Nb20X20 (X = v or Cr) refractory high-entropy alloys," *International Journal of Refractory Metals and Hard Materials*, 47, 131–138, 2014,

[22] C. M. Lin, C. C. Juan, C. H. Chang, C. W. Tsai and J. W. Yeh, "Effect of Al addition on mechanical properties and microstructure of refractory AlxHfNbTaTiZr alloys," *Journal of Alloys and Compounds*, 624, 100–107, 2015,

[23] O. N. Senkov, D. B. Miracle, K. J. Chaput and J. P. Couzinie, "Development and exploration of refractory high entropy alloys - A review," *Journal of Materials Research*, 33 (19), 3092–3128, 2018,

[24] L. Qi and D. C. Chrzan, "Tuning ideal tensile strengths and intrinsic ductility of bcc refractory alloys," *Physical Review Letters*, 112 (11), 1–5, 2014,

[25] G. Dirras, L. Lilensten, P. Djemia *et al.*, "Elastic and plastic properties of as-cast equimolar TiHfZrTaNb high-entropy alloy," *Materials Science and Engineering: A*, 654, 30–38, 2016,

[26] S. Sheikh, S. Shafeie, Q. Hu *et al.*, "Alloy design for intrinsically ductile refractory high-entropy alloys," *Journal of Applied Physics*, 120 (16), 164902, 2016,

[27] Y. D. Wu, Y. H. Cai, T. Wang *et al.*, "A refractory Hf25Nb25Ti25Zr25 high-entropy alloy with excellent structural stability and tensile properties," *Materials Letters*, 130, 277–280, 2014,

[28] H. Huang, Y. Wu, J. He *et al.*, "Phase-Transformation Ductilization of Brittle High-Entropy Alloys via Metastability Engineering," *Advanced Materials*, 29 (30), 1–7, 2017,

[29] Y. Tong, S. Zhao, H. Bei, T. Egami, Y. Zhang and F. Zhang, "Severe local lattice distortion in Zr- and/or Hf-containing refractory multi-principal element alloys," *Acta Materialia*, 183, 172–181, 2020,

[30] F. Lukac, M. Dudr, R. Musalek *et al.*, "Spark plasma sintering of gas atomized high-entropy alloy HfNbTaTiZr," *Journal of Materials Research*, 33 (19), 3247–3257, 2018,

[31] M. Wang, Z. L. Ma, Z. Q. Xu and X. W. Cheng, "Designing VxNbMoTa refractory high-entropy alloys with improved properties for high-temperature applications," *Scripta Materialia*, 191, 131–136, 2021,

[32] L. R. Owen, E. J. Pickering, H. Y. Playford, H. J. Stone, M. G. Tucker and N. G. Jones, "An assessment of the lattice strain in the CrMnFeCoNi high-entropy alloy," *Acta Materialia*, 122, 11–18, 2017,

[33] L. Owen, N. Jones, H. Stone and H. Playford, "Separation of static and dynamic displacements in the CrMnFeCoNi high entropy alloy," *Acta Materialia*, 262, 119164, Jan. 2024,

[34] H. Song, F. Tian, Q. M. Hu *et al.*, "Local lattice distortion in high-entropy alloys," *Physical Review Materials*, 1 (2), 23404, 2017,

[35] L. R. Owen and N. G. Jones, "Quantifying local lattice distortions in alloys," *Scripta Materialia*, 187, 428–433, 2020,

[36] L. Y. Tian, G. Wang, J. S. Harris, D. L. Irving, J. Zhao and L. Vitos, "Alloying effect on the elastic properties of refractory high-entropy alloys," *Materials and Design*, 114, 243–252, 2017,

[37] H. Ge and F. Tian, "A Review of Ab Initio Calculation on Lattice Distortion in High-Entropy Alloys," *Jom*, 71 (11), 4225–4237, 2019,

[38] L. R. Owen and N. G. Jones, "Lattice distortions in high-entropy alloys," *Journal of Materials Research*, 33 (19), 2954–2969, 2018,

[39] C. Lee, G. Song, M. C. Gao *et al.*, "Lattice distortion in a strong and ductile refractory high-entropy alloy," *Acta Materialia*, 160, 158–172, 2018,

[40] S. Mu, S. Wimmer, S. Mankovsky, H. Ebert and G. M. Stocks, "Influence of local lattice distortions on electrical transport of refractory high entropy alloys," *Scripta Materialia*, 170, 189–194, 2019,

[41] B. Chen, S. Li, H. Zong, X. Ding, J. Sun and E. Ma, "Unusual activated processes controlling dislocation motion in body-centered-cubic high-entropy alloys," *Proceedings of the National Academy of Sciences of the United States of America*, 117 (28), 16199–161206, 2020,

[42] C. Lee, F. Maresca, R. Feng *et al.*, "Strength can be controlled by edge dislocations in refractory high-entropy alloys," *Nature Communications*, 12 (1), 5474, 2021,

[43] F. Wang, G. H. Balbus, S. Xu *et al.*, "Multiplicity of dislocation pathways in a refractory multiprincipal element alloy," *Science*, 370 (6512), 95–101, 2020,

[44] S. I. Rao, C. Varvenne, C. Woodward *et al.*, "Atomistic simulations of dislocations in a model BCC multicomponent concentrated solid solution alloy," *Acta Materialia*, 125, 311–320, 2017,

[45] B. Chen, S. Li, J. Ding, X. Ding, J. Sun and E. Ma, "Correlating dislocation mobility with local lattice distortion in refractory multi-principal element alloys," *Scripta Materialia*, 222 (August 2022), 115048, 2023,

[46] G. D. Samolyuk, Y. N. Osetsky, G. M. Stocks and J. R. Morris, "Role of Static Displacements in Stabilizing Body Centered Cubic High Entropy Alloys," *Physical Review Letters*, 126 (2), 2019, Jan. 2021,

[47] K. Jasiewicz, J. Tobola and B. Wiendlocha, "Local distortions of the crystal structure and their influence on the electronic structure and superconductivity of (TaNb)0.67(HfZrTi)0.33 high-entropy alloy," 224505, 1–11, 2023.

[48] P. Koželj, S. Vrtnik, A. Jelen *et al.*, "Discovery of a Superconducting High-Entropy Alloy," *Physical Review Letters*, 113 (10), 107001, Sep. 2014,

[49] A. Béché, J. L. Rouvière, J. P. Barnes and D. Cooper, "Dark field electron holography for strain measurement," *Ultramicroscopy*, 111 (3), 227–238, 2011,

[50] Y. Zou, S. Maiti, W. Steurer and R. Spolenak, "Size-dependent plasticity in an Nb25Mo25Ta 25W25 refractory high-entropy alloy," *Acta Materialia*, 65, 85–97, 2014,

[51] V. B. Ozdol, C. Gammer, X. G. Jin *et al.*, "Strain mapping at nanometer resolution using advanced nano-beam electron diffraction," *Applied Physics Letters*, 106 (25), Jun. 2015,

[52] M. Hÿtch, C. Gatel, F. Houdellier, E. Snoeck and K. Ishizuka, "Darkfield electron holography for strain mapping at the nanoscale," *Microscopy and Analysis*, (26), 6–10, 2012.

[53] H. S. Oh, D. Ma, G. P. Leyson *et al.*, "Lattice distortions in the FeCoNiCrMn high entropy alloy studied by theory and experiment," *Entropy*, 18 (9), 321, 2016,

[54] Y.-Y. Tan, M.-Y. Su, Z.-C. Xie *et al.*, "Chemical composition dependent local lattice distortions and magnetism in high entropy alloys," *Intermetallics*, 129 (October 2020), 107050, Feb. 2021,

[55] Y. Y. Tan, T. Li, Y. Chen *et al.*, "Uncovering heterogeneity of local lattice distortion in TiZrHfNbTa refractory high entropy alloy by SR-XRD and EXAFS," *Scripta Materialia*, 223, 115079, 2023,

[56] E. Takeshi and S. J. Billinge, "The Method of Total Scattering and Atomic Pair Distribution Function Analysis," in *Pergamon Materials Series*, vol. 16, Elsevier Ltd, 2012, pp. 55–111, ISBN: 9780080971339.

[57] D. A. Keen, "A comparison of various commonly used correlation functions for describing total scattering," *Journal of Applied Crystallography*, 34 (2), 172–177, 2001,

[58] C. L. Farrow, P. Juhas, J. W. Liu *et al.*, "PDFfit2 and PDFgui: Computer programs for studying nanostructure in crystals," *Journal of Physics Condensed Matter*, 19 (33), 335219, 2007,

[59] P. Juhás, C. L. Farrow, X. Yang, K. R. Knox and S. J. Billinge, "Complex modeling: A strategy and software program for combining multiple information sources to solve ill posed structure and nanostructure inverse problems," *Acta Crystallographica Section A: Foundations and Advances*, 71, 562–568, 2015,

[60] S. Y. Chen, Y. Tong, K. K. Tseng *et al.*, "Phase transformations of HfNbTaTiZr high-entropy alloy at intermediate temperatures," *Scripta Materialia*, 158, 50–56, 2019,

[61] A. C. Dippel, H. P. Liermann, J. T. Delitz *et al.*, "Beamline P02.1 at PETRA III for high-resolution and high-energy powder diffraction," *Journal of Synchrotron Radiation*, 22, 675–687, 2015,

[62] Z. Hegedüs, T. Müller, J. Hektor *et al.*, "Imaging modalities at the Swedish Materials Science beamline at PETRA III," *IOP Conference Series: Materials Science and Engineering*, 580 (1), 2019,

[63] J. Kieffer, V. Valls, N. Blanc and C. Hennig, "New tools for calibrating diffraction setups," *Journal of Synchrotron Radiation*, 27, 558–566, 2020,

[64] A. C. Hannon, "Results on disordered materials from the GEneral Materials diffractometer, GEM, at ISIS," *Nuclear Instruments and Methods in Physics Research, Section A: Accelerators, Spectrometers, Detectors and Associated Equipment*, 551 (1), 88–107, 2005,

[65] W. G. Williams, R. M. Ibberson, P. Day and J. E. Enderby, "GEM - General Materials Diffractometer at ISIS," *Physica B: Condensed Matter*, 241-243, 234–236, 1997,

[66] B. H. Toby and R. B. Von Dreele, "GSAS-II: The genesis of a modern open-source all purpose crystallography software package," *Journal of Applied Crystallography*, 46 (2), 544–549, 2013,

[67] H. M. Rietveld, "A profile refinement method for nuclear and magnetic structures," *Journal of Applied Crystallography*, 2 (2), 65–71, 1969,

[68] P. Juhás, T. Davis, C. L. Farrow and S. J. Billinge, "PDFgetX3: A rapid and highly automatable program for processing powder diffraction data into total scattering pair distribution functions," *Journal of Applied Crystallography*, 46 (2), 560–566, 2013,

[69] A. Soper, "GudrunN and GudrunX: Programs for Correcting Raw Neutron and X-ray Diffraction Data to Differential Scattering Cross Section," *RAL Report RAL-TR-2011-013*, 1–151, 2011.

[70] D. Olds, C. N. Saunders, M. Peters, T. Proffen, J. Neuefeind and K. Page, "Precise implications for real-space pair distribution function modeling of effects intrinsic to modern time-of-flight neutron diffractometers," *Acta Crystallographica Section A: Foundations and Advances*, 74 (4), 293–307, 2018,

[71] O. N. Senkov, S. Gorsse and D. B. Miracle, "High temperature strength of refractory complex concentrated alloys," *Acta Materialia*, 175, 394–405, 2019,

[72] L. M. Peng, G. Ren, S. L. Dudarev and M. J. Whelan, "Debye-Waller factors and absorptive scattering factors of elemental crystals," *Acta Crystallographica Section A: Foundations of Crystallography*, 52 (3), 456–470, 1996,

[73] M. Shankar Narayana, N. Gopi Krishna and D. B. Sirdeshmukh, "X-ray determination of Debye-Waller factors and Debye temperatures of h.c.p. elements Ti, Zr, Ru, Tm, Hf," *Acta Crystallographica Section A: Foundations of Crystallography*, 57 (2), 217–218, 2001,

[74] E. Purushotham and N. Gopi Krishna, "Mean square amplitudes of vibration and associated Debye temperatures of rhenium, osmium and thallium," *Physica B: Condensed Matter*, 405 (16), 3308–3311, 2010,

[75] F. Meng, W. Zhang, Z. Zhou *et al.*, "Charge transfer effect on local lattice distortion in a HfNbTiZr high entropy alloy," *Scripta Materialia*, 203, 114104, 2021,

[76] L. Casillas-Trujillo, B. Osinger, R. Lindblad *et al.*, "Experimental and theoretical evidence of charge transfer in multi-component alloys-how chemical interactions reduce atomic size mismatch," *Materials Chemistry Frontiers*, 5 (15), 5746–5759, 2021,

[77] A. Manzoni, H. Daoud, R. Völkl, U. Glatzel and N. Wanderka, "Phase separation in equiatomic AlCoCrFeNi high-entropy alloy," *Ultramicroscopy*, 132, 212–215, 2013,

[78] B. Gorr, M. Azim, H. J. Christ *et al.*, "Microstructure Evolution in a New Refractory High-Entropy Alloy W-Mo-Cr-Ti-Al," *Metallurgical and Materials Transactions A: Physical Metallurgy and Materials Science*, 47 (2), 961–970, 2016,

[79] M. Wang, Z. Ma, Z. Xu and X. Cheng, "Microstructures and mechanical properties of HfNbTaTiZrW and HfNbTaTiZrMoW refractory high-entropy alloys," *Journal of Alloys and Compounds*, 803, 778–785, 2019,

[80] V. F. Sears, "Neutron scattering lengths and cross sections," *Neutron News*, 3 (3), 26–37, Jan. 1992,

[81] W. A. Sławiński, "Calculation of pair distribution functions for multiphase systems," *Journal of Applied Crystallography*, 51 (3), 919–923, Jun. 2018,

[82] M. Todai, T. Nagase, T. Hori, A. Matsugaki, A. Sekita and T. Nakano, "Novel TiNbTaZrMo high-entropy alloys for metallic biomaterials," *Scripta Materialia*, 129, 65–68, 2017,

[83] C. Li, S. Chen, H. Tang, J. Zhang, J. Liu and Y. Wu, "Dendrite structure-induced tunable plastic deformation behavior in (Ti-V-Cr)100-xWx refractory high entropy alloys," *International Journal of Refractory Metals and Hard Materials*, 116 (May), 106329, Nov. 2023,

[84] D. Ikeuchi, D. King, K. Laws *et al.*, "Cr-Mo-V-W: A new refractory and transition metal high-entropy alloy system," *Scripta Materialia*, 158, 141–145, Jan. 2019,

[85] D. Patel, M. D. Richardson, B. Jim, S. Akhmadaliev, R. Goodall and A. S. Gandy, "Radiation damage tolerance of a novel metastable refractory high entropy alloy V2.5Cr1.2WMoCo0.04," *Journal of Nuclear Materials*, 531, 152005, 2020,